ON-ORBIT RESIDENT SPACE OBJECT (RSO) DETECTION USING COMMERCIAL GRADE STAR TRACKERS

SAMUEL CLEMENS

A THESIS SUBMITTED TO THE FACULTY OF GRADUATE STUDIES IN PARTIAL FULFILLMENT OF THE REQUIREMENTS FOR THE DEGREE OF MASTER OF SCIENCE

GRADUATE PROGRAM IN EARTH AND SPACE SCIENCE
YORK UNIVERSITY
TORONTO, ONTARIO

MAY 2019

Abstract

The resident space object (RSO) population, including both functioning satellites and on-orbit debris, has grown to the point where dedicated ground and space-based networks are needed to maintain up-to-date catalogues of their orbits. Current tracking efforts are effective but some RSOs can go weeks without having their orbits updated, making estimates of their positions very inaccurate and effectively useless. I propose complementing current tracking efforts using commercial-grade star trackers (popular attitude determination sensors for satellites). This proposal is a novel approach that has not been implemented before. To determine their feasibility for RSO detection, a simulator was developed to estimate the detection rates of star trackers. Detection rates vary greatly but can exceed 1,200 RSOs/day (over 6% of the catalogued population). More research needs to be done, but these results, paired with their low costs, suggest that star trackers may be a cost-effective means to complement the current tracking networks.

Acknowledgements

I would like to express my great appreciation to my supervisor, Dr. Regina Lee, for her guidance, patience, help and encouragement through my master's degree. I could not have accomplished what I have without her help. I would also like to thank Paul Harrison and Warren Soh from Magellan Aerospace and Dr. Lauchie Scott from Defence Research and Development Canada for their advice, instruction and help whenever I needed it. Their guidance has been invaluable to me.

I want to thank all my friends at York University who helped me through both my undergraduate and master's degrees and who helped make my time at York a great experience. I want to specifically thank those who worked with me in the Nanosatellite Research Laboratory. Whether it was letting me bounce ideas off of them, giving advice or providing a welcome distraction from my work, they played an important role in my time at York.

Special thanks to Jessie Lott for his instruction and to Dr. Steve West for his wisdom and advice over the years.

Finally, I am particularly grateful for the love and support of my friends, family and most of all my parents. I would not be where I am today if it weren't for the constant love and encouragement that I receive from them.

Table of Contents

Abstract ..... **ii**
Acknowledgements ..... **iii**
Table of Contents ..... **iv**
List of Tables ..... **vi**
List of Figures ..... **vii**
List of Acronyms ..... **viii**
List of Symbols ..... **ix**
Chapter 1 : Introduction **1**
1.1 Problem Statement 1
1.2 Research Objective 3
1.3 Methodology 5
Chapter 2 : Background **8**
2.1 RSO Population 8
2.2 Ground-Based Detection of RSOs 10
2.3 Space-Based Detection of RSOs 15
2.4 RSO Detection Modes 18
2.5 Visual Magnitude 20
2.6 Signal-to-Noise Ratio 23
2.6.1 Sensor Noise *23*
2.6.2 External Noise (Background Light) *24*
2.6.3 SNR Calculation *26*
2.6.4 Signal Photoelectrons *27*
2.6.5 Background Photoelectrons *28*
2.7 Star Trackers 29
Chapter 3 : Analytic Simulator Description **37**
3.1 Technical Considerations of the Analytic Simulator 43
3.1.1 Resident Space Object (RSO) Propagation *43*
3.1.2 Host Satellite and Sensor Attitude Definition *45*
3.1.3 RSO Diameter Estimation *49*
3.1.4 Sensor Field of View *51*
3.1.5 Signal-to-Noise Threshold *52*

3.2 Analytic Simulator Validation 52
Chapter 4 : Image Simulator Description 60
4.1 Technical Considerations of the Image Simulator 61
4.2 Sample Simulated Images 65
4.3 Comparison with FAI 69
Chapter 5 : RSO Detectability Analysis 74
Chapter 6 : Conclusions 82
References 88
Appendix A: Parameters for Analytic Simulator Results 93
Appendix B: Survey of Star Trackers 96

List of Tables

Table 1: Galactic star density [32] 26

Table 2: Cost, latency and sensitivity comparison of RSO detection systems 33

Table 3: Overview of Analytic Simulator Parameters 38

Table 4: List of example sensor parameters 39

Table 5: Statistics used to model RSO diameters based on RSO types 50

Table 6: RMS error in SOA, EOA, DOA times 54

Table 7: Minimum, maximum and average DOA times 54

Table 8: FAI parameters [51]–[54] 56

Table 9: RSO pixel position comparison 72

Table 10: Sample COTS star tracker parameters 75

Table 11: Simulation results of Four Different Sensor Orientations 77

Table 12: Results converted to percentages 78

Table 13: Variable parameters used for each simulation from Chapter 5 94

Table 14: Common parameters used for each simulation in Chapter 5 95

Table 15: Survey of star tracker limiting magnitude and field of view 96

List of Figures

Figure 1: Monthly Number of Objects in Earth Orbit by Object Type [3] 2

Figure 2: Spatial density of Catalogued Space Debris [7] 9

Figure 3: Map of the Space Surveillance Network [11] 13

Figure 4: Background due to the zodiacal light, Moon, and the sunlit Earth, as a function of angle between the target and the limb of the Earth or Moon. The two zodiacal light lines show the extremes of possible values [31]. 25

Figure 5: Block diagram of analytic simulator 42

Figure 6: Earth-Centred Inertial (ECI) Coordinate System 47

Figure 7: Orbital Coordinate System 47

Figure 8: Anti-Sun Coordinate System 48

Figure 9: Example of Host Satellite and Sensor Attitude Definition. (Top Left) Reference coordinate system (Orbital) and spacecraft coordinate system. (Top Right) Spacecraft coordinate system and sensor coordinate system. (Bottom) All three coordinate systems. Note sensor field of view shown in orange pointing along sensor x-axis. 49

Figure 10: Histogram of 100 000 generated RSO diameters 51

Figure 11: Error in access times 54

Figure 12: Plot of visual magnitude vs. distance for accesses and detections of the analytic simulator 57

Figure 13: Point Spread Function 64

Figure 14: Simulated Image Header 64

Figure 15: Varying Exposure Time (Left: 0.1 s, Mid: 5 s, Right: 10 s) 66

Figure 16: Earth Glow 66

Figure 17: Moon in the Field of View of a star tracker 66

Figure 18: Effect of Increased Exposure Time on Noise 67

Figure 19: Increased Hot Pixel Density (Left: 0%, Mid: 0.1%, Right: 1%) 68

Figure 20: Comparison of Real and Simulated FAI Images 71

Figure 21: Meteor 1-29 satellite [72] 72

List of Acronyms

Acronym	Description
ADC	Attitude Determination and Control
COTS	Commercial Off the Shelf
DN	Digital Number
ECI	Earth Centred Inertial
EEA	Earth Exclusion Angle
FAI	Fast Auroral Imager
FOV	Field of View
GEO	Geostationary Orbit
GEODSS	Ground-Based Electro-Optical Deep Space Surveillance
GNSS	Global Navigation Satellite System
HEO	Highly Elliptical Orbit
LEO	Low Earth Orbit
MEO	Medium Earth Orbit
RHS	Right-Handed System
RSO	Resident Space Object
SBSS	Space Based Space Surveillance
SEA	Sun Exclusion Angle
SNR	Signal-to-Noise Ratio
SSA	Space Situational Awareness
SSN	Space Surveillance Network
SST	Space Surveillance Telescope
ST	Star Tracker
TLE	Two Line Element Set

List of Symbols

Symbol	Units	Description
t_{int}	s	Integration time
μ	rad	Field of view of a single pixel
ω	rad/s	Angular velocity
m_x	-	Apparent visual magnitude of an object (Sun, RSO etc.)
p	-	Reflectivity
R	km	Radius of the RSO
V	-	Absolute visual magnitude of the RSO
r	km	Distance from the RSO to the Sun
Δ	km	Distance from the RSO to the star tracker
ϕ	rad	Solar phase angle
F	-	Solar phase angle function
β	-	Mixing coefficient for specular and diffuse components of visual magnitude
ph	-	Photons
e^-	-	Electrons
δ_x	ph or e^-	Noise
N_{DC}	e^-/s	Dark current production rate
e_x	ph	Incident photons
SNR	-	Signal-to-Noise Ratio
E_{RSO}	ph/s/m^2	Irradiance
QE	-	Quantum efficiency
τ	-	Optical transmittance loss
A	m^2	Aperture area
t_{sig}	s	Signal integration time
L_b	ph/s/m^2/sr	Radiance
S_b	mv/arcsec^2	Surface brightness of the background sky
n	-	Number of pixels on one side of a detector
x	m	Length of one side of a pixel
f	m	Focal length of the sensor

Chapter 1: Introduction

1.1 Problem Statement

Space Situational Awareness (SSA) has grown increasingly important in recent years as objects begin to crowd Earth's orbit. The risk of collisions between Resident Space Objects (RSOs) has become much greater. An impact between an RSO and an active satellite threatens to disable or even destroy the active satellite. An impact between any two RSOs (active satellite or not) threatens to further increase the population of RSOs by creating fragmentation debris. The growing RSO population is a challenge for those attempting to track RSOs and assess the risk that they pose, as well as for mission planners and operators who need to factor in the growing risk of collisions and even the risk of malicious encounters from controlled RSOs.

Figure 1 shows how the RSO population has been growing since the 1950s. Spacecraft, mission-related debris and rocket bodies have been increasing at approximately the same rate while fragmentation debris has been increasing at least twice as fast. Two large increases in the fragmentation debris population can be seen, one in 2007 and the other in 2009. In 2007, China conducted an anti-satellite missile test and destroyed a Chinese weather satellite. In 2009 there was a collision between two satellites, Iridium 33 and Cosmos 2251. Both of these events caused a large increase in the amount of debris in orbit around Earth. Along with these two events, another large increase in the debris population occurred on March 27, 2019 (not shown in Figure 1) when India conducted an anti-satellite missile test. The test resulted in at least 400 new pieces of orbital debris, some of which had an apogee (the highest point a satellite reaches above the Earth's surface in its orbit) beyond the International Space

Station (ISS). This missile test increased the risk of impact between debris and the ISS by 44% [1]. NASA estimates that there are over 21,000 debris objects greater than 10 cm in orbit around Earth, approximately 500,000 objects between 1 cm and 10 cm and over 100 million debris objects smaller than 1 cm [2].

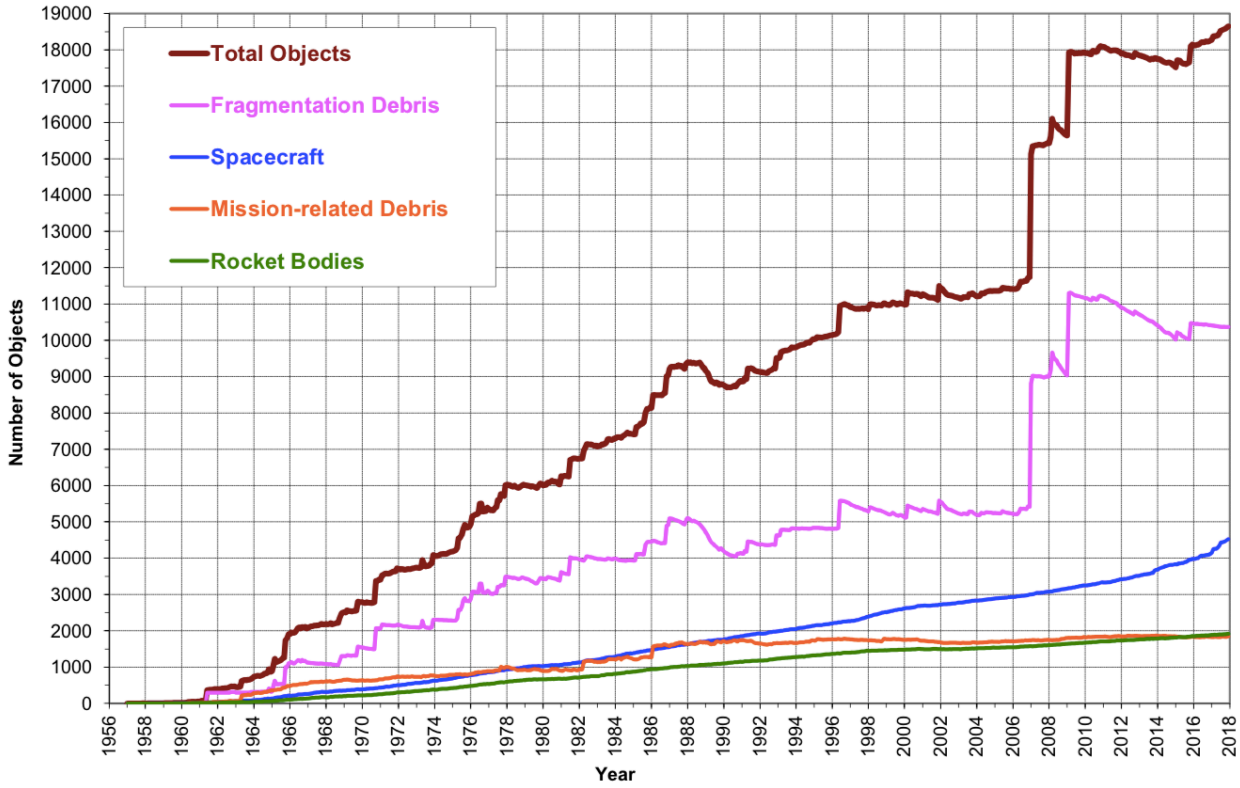

Figure 1: Monthly Number of Objects in Earth Orbit by Object Type [3]

The growing need to detect and track RSOs has been met by both ground-based and space-based efforts. These efforts will be discussed further in Chapter 2. Despite all of the efforts to track RSOs, there are still gaps in the temporal and spatial coverage provided by these networks and sensors. One possible solution to reducing these gaps is found in star trackers, a popular sensor for attitude determination and control (ADC) that is currently being used on many satellites in orbit today. A star tracker is a camera that images the stars and can determine the attitude of the satellite by the position of the stars in the image. If these sensors are capable of imaging RSOs, then they could

be dual-purposed to image RSOs when not being used for ADC or even used as dedicated RSO tracking sensors. After an image or series of images from a star tracker is determined to contain an RSO, processing would be required to determine the orbital parameters of the RSO. Depending on the mission architecture, this processing may be done on board or on the ground (or a combination of the two). If star trackers currently in orbit could be dual-purposed for RSO detection, then there is a multitude of sensors just waiting to be used for RSO tracking (and more on the way as more satellites with star trackers are launched). The benefit of using star trackers for RSO detection and tracking is that they are already flight-qualified (proven to be suitable for use in the space environment). There would be no new hardware that needed to go through the design and flight qualification process which would greatly reduce the time, risk and cost of adding new SSA sensors. Dedicated sensors could be launched and placed in strategic orbits, reducing the gaps in SSA coverage without requiring large research and development costs, time and risk. In either case (dual-purposed or dedicated), the use of star trackers for RSO detection and tracking would allow a large network of space-based sensors to be formed and complement existing ground and space-based sensors, contributing to the global SSA catalogue.

1.2 Research Objective

The aim of this research is to determine the feasibility of using commercial-off-the-shelf (COTS) star trackers for RSO detection for the purpose of complementing the ground and space-based RSO detection efforts that are currently in use. For star trackers to be a feasible source for RSO detections they must contribute something that the current tracking networks do not. Detecting RSOs that are already effectively

covered by existing networks does not provide any improvements to SSA. Star trackers must be able to fill in some of the temporal gaps that exist. For a star tracker to be feasible for RSO detection it needs to be able to detect the portions of the RSO population that are not updated on a regular basis. Determining a star tracker's feasibility for RSO detection requires several steps:

- Assess the ability of star trackers to detect RSOs
- Identify the RSOs that are not updated on a regular basis
- Determine the ideal orbital and mission parameters for a star tracker to best fill in those gaps
- Assess the star tracker's ability to fill in the identified gaps given the ideal parameters

The first step in determining star tracker's feasibility is to assess whether or not star trackers have the sensitivity to detect the general RSO population given the size and velocity of RSOs and the parameters (aperture size, focal length, etc.) of star trackers. If star trackers are not sensitive enough to detect the general RSO population then they should not be considered for use in detecting the un-updated portions of the RSO population. The second step is to identify the RSOs that belong to the un-updated portion of the population. The un-updated RSOs need to be examined to determine approximately what orbits they are in (and if there are groups of un-updated RSOs). It will also be important to prioritize the RSOs and determine which ones are the most important to update (e.g., an RSO crossing the orbit of the International Space Station may be a high priority due to the threat of collision). The third step after the un-updated RSOs have been identified is to determine the ideal mission parameters (orbit, star

tracker orientation, etc.) that will maximize the effectiveness of the star tracker. The "ideal" parameters would be based on the number of these un-updated RSOs that can now be updated, their priority and how frequently they get updated (once a week, once a day, etc.). The final step is to determine if, given the ideal mission parameters, enough un-updated RSOs can be detected to make the star tracker an effective source of RSO detections.

The focus of this thesis is on the first step of establishing a COTS star tracker's ability to detect the general RSO population and a baseline goal of 10 RSO detections per star tracker per day from a favourable orbit has been set to establish this. A detection rate of 10 RSOs per day from a favourable orbit (i.e., an orbit that is highly populated with RSOs) demonstrates that star trackers have the sensitivity to detect even just a small portion of the general RSO population. If the star tracker is unable to detect any objects from a favourable orbit, then it is not likely to have the ability to detect objects in a specialized orbit for detecting un-updated RSOs. If, however, this baseline goal can be met, then it may be possible for the use of star trackers to be extended to the detection of the un-updated portion of the RSO population.

1.3 Methodology

In order to determine the feasibility of a COTS star tracker for RSO detection, a simulator was developed to estimate the detection rates of star trackers. This simulator is called the "Analytic Simulator" throughout this thesis. The simulator was written in MATLAB. It uses the two-line element sets (TLEs) for the RSOs, as well as a TLE for the host satellite of the star tracker and propagates their orbits to determine which RSOs cross the field of view of the star tracker and of those RSOs that cross the field of

view, which are above a certain signal-to-noise ratio threshold to be considered detectable. The simulator has many variables that are under the control of the user, such as the host satellite for the star tracker, the orientation of the star tracker, the date and duration of the simulation, and the parameters for the star tracker itself. These variables allow the simulator to be used to estimate detection rates for any number of scenarios.

A second MATLAB simulator (called the “Image Simulator”) was developed to generate simulated images, showing what a star tracker would output when taking an image. This simulator was developed mainly for the testing of future work. Currently, star tracker images are not readily available. Full images are not required to be downloaded to Earth from the star tracker in order to determine its attitude. Because of this, another source of star tracker images is required. This MATLAB image simulator is intended to be a source of star tracker images that can be used for algorithm testing to further the prospect of using COTS star trackers for SSA. Once an image is taken by a star tracker it needs to be determined whether the image contains an RSO or not. After an RSO has been detected within an image, its orbital parameters can be determined; it can be identified (if already catalogued); and it can even be characterized as controlled or uncontrolled by observing the light curve (the brightness with respect to time) of the RSO from successive images. All of these results (detection, orbit determination, identification and characterization) require different algorithms and data to be applied to and taken from the images. The image simulator serves as a source of star tracker images to be used for the development of these algorithms.

The remainder of this thesis is dedicated to background discussion of RSOs, space situational awareness and star trackers; descriptions of the analytic and image simulators; discussion of the results of the analytic simulator and the detection rates it provides and finally, conclusions based on these results.

Chapter 2: Background

2.1 RSO Population

The term Resident Space Object (RSO) encompasses various classes of objects. The term refers to active satellites, inactive satellites or some sort of debris. Debris may refer to:

- Mission-Related Debris — Objects that are intentionally discarded when a satellite is deployed or during normal operations of a satellite (lens caps, empty propellant tanks, etc.)
- Rocket Bodies – Spent upper stage rockets used to deploy satellites
- Fragmentation Debris — The result of collisions, explosions or aerodynamic forces when an object is re-entering Earth's atmosphere
- Anomalous/Deterioration Debris — The result of spacecraft deterioration over time (pieces/parts that separate from spacecraft, paint flaking, etc.)
- Slag/NaK/Other — Small particles created from solid rocket motors firing are called slag (Al_2O_3). Sodium-potassium (NaK) droplets were released from a Soviet Union spacecraft back in the 70s and 80s and contribute to orbital debris particles. Slag and NaK can be micrometer-sized or mm- to cm- sized particles [4], [5]

Today, 63% of RSOs are debris, 25% are active/inactive satellites and 11% are rocket bodies [6].

Figure 2 shows the spatial density of RSOs up to an altitude of 50,000 km. Spikes in the density can be seen from 0 – 2,000 km (Low Earth Orbit, LEO), 19,000 km and 35,700 km (Geostationary Orbit, GEO). LEO is clearly the most densely populated area of space. This data is from 1994. The spatial density of objects in orbit around Earth will only have grown since 1994.

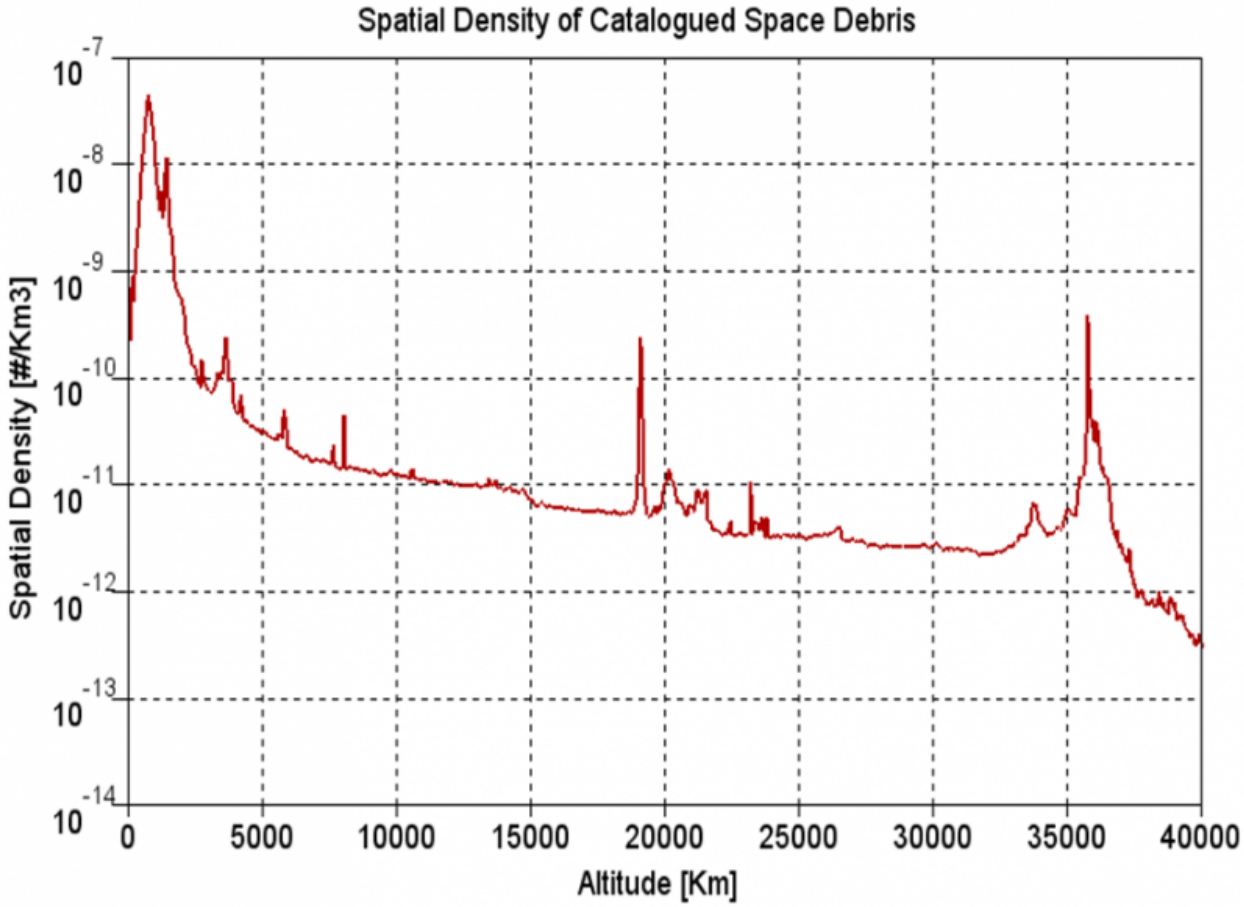

Figure 2: Spatial density of Catalogued Space Debris [7]

The Joint Functional Component Command for Space (JFCC Space) is a component of U.S. Strategic Command and keeps a catalog of RSOs both in orbit and ones that have already decayed on the website space-track.org. A two-line element set (TLE) for many of the catalogued RSOs that are in orbit is provided by space-track.org (some TLEs are kept secret for security purposes). TLEs can only be used to determine

the position and velocity of an RSO for a short window around the time it is referenced to (its epoch). As the time between the epoch and the time that the position estimation is desired grows, the estimation quickly becomes very inaccurate. TLEs can only be used to determine positions of RSOs within approximately a week of their epoch and therefore the TLE of an RSO constantly needs to be updated to provide accurate estimations of its position. According to this catalog (as of January 22, 2019) there are approximately 19,451 RSOs larger than 10 cm currently in orbit. The typical minimum size of objects tracked and catalogued on space-track.org is 10 cm. Of those 19,451 RSOs, 12,185 (63%) of them are debris, 2,191 (11%) of them are rocket bodies, 4,941 (25%) are payloads and 134 (< 1%) are unassigned [6]. Some of the RSOs were produced purposefully (rocket bodies, payloads and mission related debris) and "belong" in space, while others were produced accidentally (deterioration debris and fragmentation debris). Despite the varying nature of catalogued RSOs, it is clear that the majority are indirect side effects of space operations (fragmentation or other forms of debris).

2.2 Ground-Based Detection of RSOs

Detection of RSOs is made with ground-based sensors or space-based sensors. The majority of efforts to-date have come from ground-based sensors, but space-based sensors provide a unique vantage point from which to detect RSOs and the use of space-based sensors has been increasing in recent years.

There are two types of sensors used for ground-based detection of RSOs, optical sensors and radar sensors. In general, electro-optical sensors are used for objects above 5,000 km and radar sensors are used for lower altitude observations. The

strength of the received signal from radar sensors falls off at $\frac{1}{r^4}$, where r is the distance to the object, causing the effectiveness of radar sensors to quickly decrease with altitude [4]. Despite their short range, an advantage of radar sensors is that they can operate in all kinds of weather as well as day or night. Optical sensors on the other can only operate on clear, dark nights. Both parabolic radar antennas and phased array antennas have been used in the detection of RSOs.

Radar measurements are able to determine the following parameters of an RSO:

- orbital elements
- attitude
- size and shape
- orbital lifetime
- ballistic coefficient
- object mass
- material properties

Again, one of the disadvantages of optical measurements is that clear, dark nights are required for detecting RSOs. Cloud coverage, fog, background light and airglow make it difficult for optical instruments to detect RSOs. Optical measurements in LEO are limited to an hour or two after sunset or before sunrise, while measurements in HEO (High Earth Orbit) can usually be continued through the night. Generally, telescopes with wide fields of view are wanted because that allows the sensor to survey more of the sky. However, telescopes with wide fields of view generally have a lower limiting magnitude and are not able to detect faint objects. To detect objects in GEO

smaller than 1m, a telescope with a limiting magnitude of 17.1 is required [8]. A detailed description of limiting magnitude is given in Section 2.5 .

As stated above, JFCC Space's Satellite Catalogue typically records objects with a minimum diameter of 10 cm. According to the ESA, a ground-based telescope can detect objects down to 10 cm in size in GEO and a ground-based radar can detect objects down to a few centimetres in size in LEO. These thresholds are a compromise between system cost and performance [9].

Below is summarized several of the major ground-based RSO detection efforts. The survey, however, is not comprehensive and just describes a few of the major optical sensors and systems that are in use. The Space Surveillance Network is a United States organized collection of over twenty sensors, that are both military and civilian operated [10]. The objective of the SSN is to update the JFCC Space Satellite Catalogue on space-track.org. Some of the sensors are categorized as dedicated, meaning that they belong to the Air Force Space Command (AFSPC) and are dedicated to the objective of space surveillance. Other sensors are called collateral sensors, meaning that they belong to the AFSPC, but space surveillance is a secondary objective they have. The final category of SSN sensors is called contributing sensors, meaning that they belong to someone other than the AFSPC but provide data to the SSN [4], [10]. The SSN consists of phased-array radars, conventional radars and electro-optical sensors (both ground and space-based) [4]. The SSN tracks objects down to a diameter of approximately 10 cm [6]. Figure 3 is a map of the SSN as of 2017. The type of sensor and its relationship to the SSN (dedicated, collateral or

contributing) is indicated in the figure. Note that SSN C2 refers to the command and control centres for the SSN.

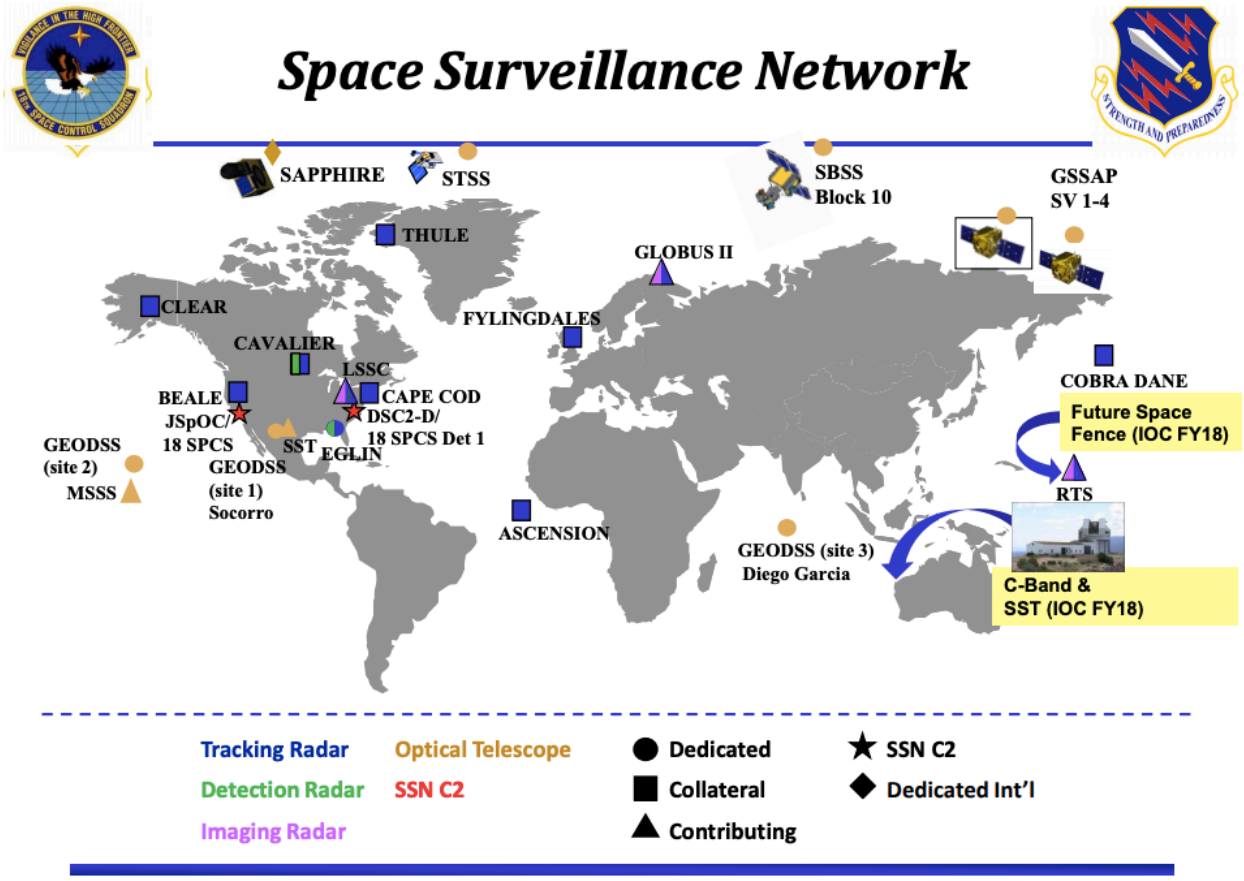

Figure 3: Map of the Space Surveillance Network [11]

Two significant ground based optical sensors for the SSN are the Ground-Based Electro-Optical Deep Space Surveillance (GEODSS) system and the Space Surveillance Telescope (SST). The GEODSS system is considered the backbone of the SSN's GEO satellite tracking capability which has been operational since the 1980s. It is a network of three different active sites located on the islands of Maui and Diego Garcia as well as near Socorro, New Mexico. Each site consists of three 1 m telescopes with a focal length of 2.15 m [12]. The SST was designed as a prototype for a new generation of ground-based optical sensors. It has a 3.5 m aperture with a focal length of 3.5 m. It was originally constructed in New Mexico but as of 2015 had begun to be

moved to Australia [12]. More recent information was unavailable, and it is unclear if it is currently operating. The SST can make up to 25,200 observations per day, twice as many as a single GEODSS telescope (12,600). However, the entire GEODSS network makes up to 113,400 observations per day (three telescopes per site). The SST is also slightly more sensitive than a GEODSS telescope. They can observe objects around magnitude 19.5 and 17.5, respectively [12].

A more comprehensive, though slightly dated (2008), reference for the SSN can be found in the NASA Handbook for Limiting Orbital Debris [4]. The majority of sensors used by the SSN are ground based. More detail on many of the SSN sites can be found in the handbook. Some of the sensors listed in the handbook have since become non-operational (MSX/SBV for example) and some that came online after 2008 (like the SST) are not listed.

The Tracking and Imaging Radar (TIRA) is a space observation radar in Germany that the ESA collaborates with for debris detection and tracking. The dish has a diameter of 34 m. TIRA has a “beam park” mode in which it stares in a fixed direction for 24 hours. This gives it a narrow 360-degree strip of the sky in which it detects objects that pass through the beam. It can detect objects as small as 2 cm at a 1,000 km range [9].

The European Incoherent Scatter Scientific Association (EISCAT) operates four different sites with 32 m radar dishes in Sweden, Norway and Finland. It is an international partnership between 10 different countries. Although its primary mission is not debris detection, dedicated space-debris computers have been developed which can run continuously and monitor LEO for debris down to a few centimeters in size [9].

The ESA operates the Optical Ground Station (OGS) in Spain. It is a 1 m optical telescope that is used for the monitoring of geostationary satellites. The telescope can detect objects down to a visual magnitude of 21 which translates to objects about 10-15 cm in size in the geostationary belt [9].

2.3 Space-Based Detection of RSOs

Space-based optical imaging has a significant advantage over ground-based optical imaging in that it is not limited by the time of day, the weather, the atmosphere or the phase of the moon. Ground-based optical sensors can only perform in clear, dark skies and are therefore limited to dark nights with good weather (no clouds). Space-based optical sensors do not have those restrictions. There are multiple space-based sensor/satellite systems that have recently been or currently are operational. A description of several major space-based systems is given below.

NEOSSAT is a Canadian microsatellite that was launched on February 5, 2013. It is approximately 800 km above the Earth's surface. The telescope on NEOSSAT has a 15 cm aperture and a 0.85-degree field of view. NEOSSAT has two main objectives. The first is Near Earth Space Surveillance (NESS) which searches for near earth asteroids. The other main objective is High Earth Orbit Space Surveillance (HEOSS) which searches for Resident Space Objects (RSO) such as satellites, rocket bodies and fragmentation debris in orbit around earth. HEOSS searches for RSOs with altitudes greater that 15,000 km (beyond LEO). NESS can detect asteroids as faint as 19.5-20 mv, while HEOSS can detect RSOs only as faint as 13.5 mv (a lower limiting magnitude due to the high angular rates at which RSOs travel). NESS uses a 100 second exposure time when taking images. Because asteroids being imaged by NESS move

much slower relative to the telescope than RSOs being imaged by HEOSS, the time that an asteroid is over a given pixel is two orders of magnitude larger than the time that an RSO is over a given pixel. This means that HEOSS likely has a much smaller exposure time than NESS (on the scale of seconds), although the exact exposure time is unsure [13]–[15]. NEOSSAT uses both a tracking mode and a stare mode to detect RSOs. In tracking mode, the sensor is slewed to point where a suspected RSO is and continues to slew to follow the RSO. In stare mode, the sensor waits for RSOs to cross its field of view. The tracking and stare modes will be described in more detail later in Section 2.4 . In both cases, NEOSSAT takes a series of images. In tracking mode, the RSO is seen as a dot which is stationary in the images while stars are seen as streaks in the images. In stare mode, all of the stars are dots in the images while the RSO can be seen as a streak which moves in successive images.

Sapphire, another Canadian satellite, was launched on board the same launch vehicle as NEOSSAT in February 2013. It detects and tracks RSOs between 6,000 km and 40,000 km above Earth while it is in a sun-synchronous near-circular dawn-dusk orbit at an altitude of ~786 km. It uses an electro-optical telescope with a 15 cm aperture and 1.4-degree field of view, which allows it to detect RSOs down to a magnitude of 15 mv. On-orbit results from Sapphire were obtained using 0.1 second and 4 second integration times. Sapphire provides valuable contributions to the SSN [16]. Sapphire operates in track mode and has as many as 1,600 observations per day [12].

The Space Based Space Surveillance (SBSS) Block 10 is an AFSPC controlled satellite dedicated to RSO detection that contributes to the SSN. It was launched in

September of 2010 into a 630 km sun-synchronous orbit and is a follow-on to the now retired Midcourse Space Experiment (MSX) satellite which was the first space-based sensor to contribute to the SSN [17]. SBSS Block 10 uses a similar sensor to the one used by the MSX satellite [18]. MSX had a sensor called the Space Based Visible Sensor (SBV), which had a 15 cm aperture telescope (1.4 x 6.6-degree field of view) mounted on a two-axis gimbal which allows the telescope to be slewed to different targets without expending time and fuel to move the entire spacecraft [19]. The SBSS satellite has a 30 cm aperture telescope and is believed to have a field of view of 2 degrees by 4 degrees and an ability to detect RSOs as faint as magnitude 16.5. It uses a similar two-axis gimbal as the SBV sensor onboard the MSX satellite and can operate in both track and stare mode like the SBV [12]. For track mode the SBV used 1 second exposure times while for stare mode it used 0.4 second exposure times [19] and SBSS may use similar exposure times. The SBSS satellite can obtain up to 12,000 observations per day (nearly ten times as many as Sapphire) [12].

The Geosynchronous Space Situational Awareness Program (GSSAP) is a constellation of four dedicated SSN satellites that monitor the geosynchronous belt. These satellites operate in near-geosynchronous orbits but have the capability to perform Rendezvous and Proximity Operation (RPO). RPO allows the satellites to maneuver close to an RSO of interest to better characterize the RSO. No information on the sensors or exposure times used by the GSSAP satellites could be found [20].

The Space Tracking and Surveillance System (STSS) (originally called SBIRS-Low) is composed of two U.S. satellites (STSS DEMO 1 and 2) which are both dedicated SSN sensors. STSS was designed as a demonstration for on-orbit missile

tracking. The satellites orbit at an altitude of 1,350 km with an inclination of 58 degrees. The follow up program has been cancelled but the two satellites exceeded their planned two-year lifespan. They were expected to operate into 2017 but it is unclear if they are still operational [21].

The Space-Based Infrared System (SBIRS) is another U.S. missile defense system (but does not contribute to the SSN like STSS does). Currently, it consists of three HEO sensors and four GEO satellites with another HEO sensor soon to become operational and two more GEO satellites planned in the future. The system uses infrared sensors to detect missiles that have been launched [22].

Another form of space-based measurement of RSOs is called *in situ* measurements and is described in the NASA Handbook for Limiting Orbital Debris [4]. This method observes the effects of impacts on spacecraft surfaces after they have returned to Earth. *In situ* measurements are accomplished on spacecraft that are intentionally put in orbit in order to study the effects of RSO impacts (like the Long Duration Exposure Facility (LDEF)). In the past, *in situ* measurements were also accomplished by inspecting the surfaces of the space shuttles after they returned to Earth [4].

2.4 RSO Detection Modes

There are two modes in which a sensor monitors RSOs: tracking mode and stare mode. In tracking mode, the sensor slews to a known position of an RSO and continues to slew to keep the RSO within the field of view of the sensor. In stare mode, the sensor points in a fixed direction and detects objects as they pass through the field of view of the sensor. Stare mode is sometimes called sidereal mode when the sensor points in a

fixed direction with respect to the stars. A sensor may be in stare mode but cannot necessarily be considered sidereal. For example, when a sensor on a spacecraft is fixed relative to the spacecraft's orientation it is operating in stare mode. If, however the spacecraft orientation is not fixed relative to the stars then the sensor is also not fixed relative to the stars and cannot be considered to be in sidereal mode.

The exposure time for an optical sensor operating in stare mode is critical. Too long of an exposure will cause background noise to dominate the signal and the RSO will be lost in noise. Too short of an exposure time will cause the signal to be too weak and not distinguishable from the noise. The ideal exposure time is related to the relative velocity of the RSO with respect to the sensor. The ideal exposure time is the time that it takes the RSO to traverse a single pixel of the detector. As long as the RSO remains over that pixel, the signal is increasing. But when the RSO moves to another pixel, the signal stops increasing while the noise continues to increase. The ideal integration time is shown below:

$$t_{int} = \frac{\mu}{\omega} \tag{1}$$

where μ is the field of view of a single pixel (pixel dimension / focal length), ω is the angular velocity of the RSO with respect to the sensor in radians per second and t_{int} is in seconds [23].

For a sensor operating in track mode, an RSO will appear as a dot in the image while all of the stars in the image streak in the same direction. For a sensor operating in stare mode, all of the stars will streak in the same direction (similar to track mode) but the RSO will also appear as a streak. The RSO streak can be distinguished from the stars because it is generally a different length and in a different direction than the stars.

The length of the streaks for both stars and RSOs depends on the relative motion between them and the sensor and the exposure time. The faster the relative motion and the longer the exposure time of a sensor, the longer the RSO and star streaks appear in an image. Often successive images are taken so that the motion of a suspected RSO can be analyzed from one image to the next to determine if it is actually an RSO or simply hot pixels showing up in different images.

2.5 Visual Magnitude

The brightness of an RSO depends on many factors (size, distance from the sensor, phase angle, reflectivity, etc.) Visual magnitude is a unitless measure of how bright an object is. Sometimes the symbol “mv” is used as a short form for “visual magnitudes” (a visual magnitude of 10 is the same as 10 mv). It is the same scale used by astronomers when classifying the brightness of astronomical objects. The visual magnitude scale is a logarithmic one, meaning that a difference in visual magnitude of 1 corresponds to a brightness factor of 2.5. Brighter objects are lower on the scale than dimmer objects. The brightest star in our sky is Sirius and has a magnitude of -1.5 (the apparent brightness of the stars varies with distance so from another view Sirius won’t necessarily be the brightest). The Sun has a visual magnitude of -26.73 while a full moon has a visual magnitude of -12.5. The faintest objects to have been observed are over a magnitude of 30 [24]. To calculate the visual magnitude of an RSO (m_{RSO}), the equation from Karttunen et al., shown below in Equations 2 and 3, was used [24]. For simplicity sake, RSOs are assumed to be spherical. The visual magnitude of the sun is denoted by m_{sun}, p is the reflectivity of the RSO (technically geometric albedo), R is the radius of the RSO in km, a is 1 AU in km, V is the absolute magnitude of the object, r is

the distance from the RSO to the Sun in km, Δ is the distance from the RSO to the star tracker in km, ϕ is the solar phase angle (the angle between the sun and the star tracker relative to the RSO) and $F(\phi)$ is the solar phase angle function.

$$V = m_{sun} - 2.5\,log\left(p\frac{R^2}{a^2}\right) \tag{2}$$

$$m_{RSO} = V + 5\,log\left(\frac{r\Delta}{a^2}\right) - 2.5\,log\big(F(\phi)\big) \tag{3}$$

Note that Equation 3 is a generic equation to calculate the visual magnitude of any object, observed from the Earth, that is reflecting light from the sun. Shell [23], Krag [25] and Hejduk [26] use simplified versions of Equations 2 and 3 above. The simplified versions are some variant of Equation 4 below.

$$m_{RSO} = m_{sun} - 2.5\,log\left(\frac{pAF(\phi)}{\Delta^2}\right) \tag{4}$$

The above equation is valid and makes assumptions based on RSOs being the same distance from the Sun as the Earth (i.e., r equals a, because they are in Earth's orbit), but it is not used in this thesis. This thesis does not use this assumption to simplify Equations 2 and 3 because these equations were being used in the simulators and the function using them needed to be verified. To verify the functions, real visual magnitudes from Mercury, Venus, Mars and Jupiter were used because visual magnitudes of RSOs in Earth's orbit was not easily accessible. To verify the function using those four planets, the assumptions about RSOs being the same distance from the Sun as the Earth cannot be used. That's why this thesis does not use the assumptions that Shell, Krag and Hejduk use.

The reflectivity and solar phase angle function can be split into specular and diffuse components. The specular and diffuse phase angle functions are shown below

in Equations 5 and 6. Shell uses equal contributions of both specular and diffuse reflectivity components, as well as equal contributions of phase angle functions, which he claims is supported by observational data. Hejduk also claims that the strictly diffuse sphere as an estimate of RSOs typically used by simulation analysists is not an accurate model. He suggests some combination of the specular and diffuse phase function components, though not necessarily equal contributions as used by Shell [26].

$$F_{spec}(\phi) = \frac{1}{4} \tag{5}$$

$$F_{diff}(\phi) = \frac{2}{3\pi}[(\pi - \phi)\cos(\phi) + \sin(\phi)] \tag{6}$$

In Equations 5 and 6, ϕ is the solar phase angle. Note that if the cross-sectional area (rather than the radius) of the RSO is being used, the phase angle functions are multiplied by $\frac{1}{\pi}$.

The reflectivity of RSOs would vary depending on the type of RSO. The latest estimate for the reflectivity of fragmentation debris is 0.175, while a value of 0.2 is often used for payloads and rocket bodies [23].

The complete equation to calculate visual magnitude when considering some combination of specular and diffuse components is shown below in Equations 7 and 8. The mixing coefficient β was added to combine the specular and diffuse components and can range from 0 to 1. A mixing coefficient of 1 gives a completely diffuse object while a mixing coefficient of 0 gives a completely specular object [26].

$$V = m_{sun} - 2.5\log\left(p\frac{R^2}{a^2}\right) \tag{7}$$

$$m_{RSO} = V + 5\log\left(\frac{\mathrm{r}\Delta}{\mathrm{a}^2}\right) - 2.5\log\left[\beta \mathrm{F}_{\mathrm{diff}}(\phi) + (1-\beta)F_{spec}(\phi)\right] \tag{8}$$

2.6 Signal-to-Noise Ratio

Signal-to-noise ratio (SNR) is the ratio between the desired signal and the background noise being measured. In this situation, the signal and noise are photoelectrons produced by the detector of the sensor. Each pixel of the detector converts incident photons to photoelectrons. The signal is produced by incident photons from an RSO. Noise can come from incident photons from background light as well as photoelectrons produced by different types of internal detector noise.

There a several different sources of noise involved in space-based imaging that make it difficult to image RSOs. Both the sensor itself and the external environment contribute to the noise in an image. The noise sources from the sensor that are considered in this study are dark current, read noise and shot noise. The external noise sources considered in this study are simply different sources of background light which include direct light from the sun, sunlight scattered through the Earth's atmosphere, sunlight reflected off the Moon's surface, stars and zodiacal light.

2.6.1 Sensor Noise

There are several types of noise that affect sensors. The noise sources that are considered in this study are dark current, read noise, shot noise and the non-uniformity in these noise sources. These are the major sources of noise that contribute to the SNR and all other noise can be safely ignored.

Dark current is produced by electrons that are created over time by thermal energy in the sensor. The electrons are captured by the detector and counted as signal. By cooling the sensor, the amount of dark current produced can be decreased. Dark current is rated as e-/pixel/sec and is modelled using a Poisson distribution [27], [28].

Dark current noise, given in the equation below, is the square root of the dark current produced for a given exposure time, where δ_{dark} is the dark current noise, N_{DC} is the dark current production rate and t_{int} is the exposure (integration) time.

$$\delta_{dark} = \sqrt{(N_{DC}) \times (t_{int})} \tag{9}$$

Readout noise is noise that is produced by the electronics of the sensor as it quantifies the electronic signal of each pixel produced by the incident photons. The majority of readout noise comes from the process of amplifying the signal [27], [29].

Shot noise (also photon or Poisson noise) is a result of the discrete nature of light. Photon flux incident on a sensor is not constant and follows a Poisson distribution. The amount of shot noise is directly related to the number of incident photons. The equation for shot noise can be seen in Equation 10 where δ_{shot} is the shot noise and e_i is the number of incident photons. An increase in the number of photons increases the SNR when considering shot noise as the only source of noise [27], [29].

$$\delta_{shot} = \sqrt{e_i} \tag{10}$$

2.6.2 External Noise (Background Light)

Background light is recorded as a surface brightness with the units of [mv/arcsec^2], where “mv” stands for visual magnitudes. Direct light from the sun that is incident on a sensor is obviously the dominant source of background light, with the Earth and Moon also providing significant contributions. Light from these three sources is dependent on the angle at which the sensor is pointed away from the source. Each of these sources have the potential to dominate a sensor and prevent any useful imaging from occurring. To prevent these sources from dominating the sensor, operators will often only take images when outside of a specified viewing exclusion angle from the

limb of a body. The Hubble Space Telescope (HST) is a good example of a sensor that uses exclusion angles. The HST uses the following exclusion angles for the Sun, the bright Earth limb, the dark Earth limb and the Moon respectively: 50 degrees, 15.5 degrees, 7.6 degrees and 9 degrees [30]. Below is a figuring showing the contribution of the Earth's bright limb and the Moon to the background sky brightness based on the viewing angle from the limb.

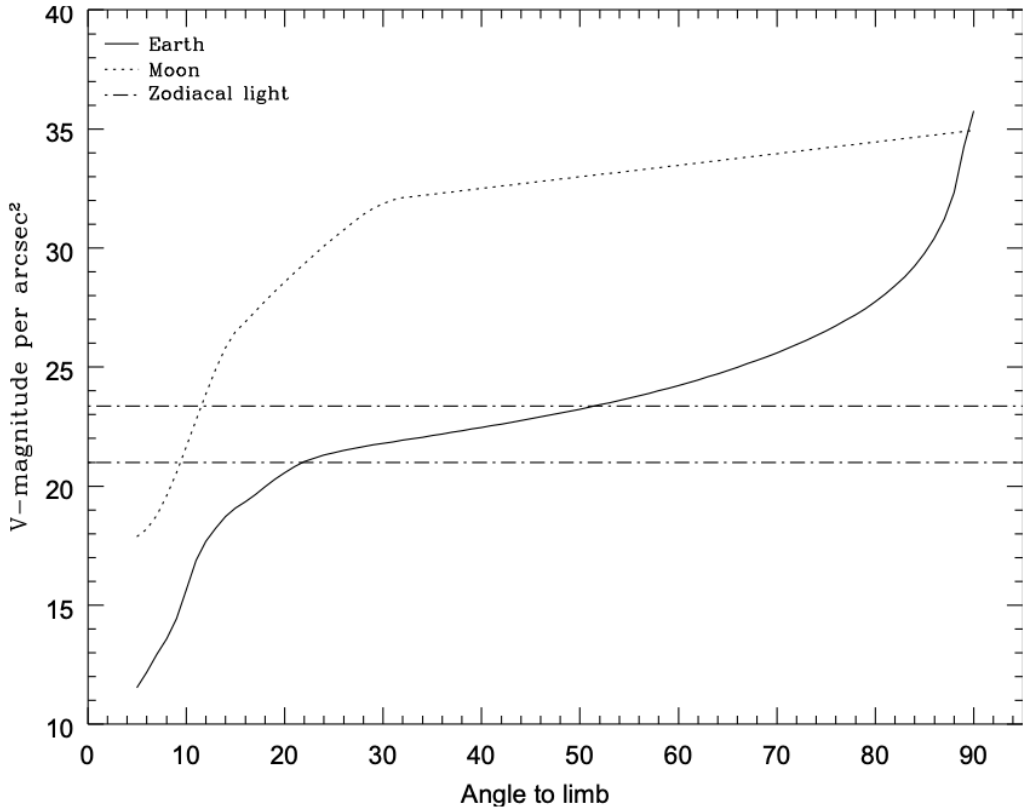

Figure 4: Background due to the zodiacal light, Moon, and the sunlit Earth, as a function of angle between the target and the limb of the Earth or Moon. The two zodiacal light lines show the extremes of possible values [31].

The stars are the next most significant source of background light. They are not distributed uniformly on the celestial sphere but are concentrated more heavily in the galactic plane. The table below is from Zakharov et al. [32] and shows the average

number of stars brighter than a given magnitude per square degree of the sky. The stellar density is much higher in the galactic plane than in the rest of the sky.

Table 1: Galactic star density [32]

Magnitude	Average star density			Magnitude	Average star density		
	entire sky	Galactic pole	Galactic plane		entire sky	Galactic pole	Galactic plane
5.0	0.05	0.04	0.08	10.0	10.4	4.68	33.2
6.0	0.15	0.13	0.32	11.0	25.5	10.6	80.0
7.0	0.47	0.35	1.32	12.0	61.2	23.2	192
8.0	1.53	0.88	4.51	13.0	139	47.6	446
9.0	4.10	1.99	12.8	14.0	297	91.2	968

Zodiacal light is light from the sun that is reflected by intra-solar system dust. The magnitude of reflected light is a function of solar phase angle. Shell [23] combines the zodiacal and stellar background lights in to a background of 22 mv/arcsec^2 and treats it as spatially uniform. He does not consider the solar phase angle or the angle from the galactic plane when using the background stellar and zodiacal lights in his calculations. This same method is adopted in this study and a combined background of 22 mv/arcsec^2 is used for the stellar and zodiacal background light.

2.6.3 SNR Calculation

The total SNR is given by the equation shown below, where $\delta_{readout}$ is the readout noise, δ_{BGShot} is the background shot noise, $\delta_{signalShot}$ is the signal shot noise, e_{BG} is the incident background photons and e_s is the incident signal photons [33]:

$$SNR = \frac{e_s}{\sqrt{\delta_{dark}^2 + \delta_{readout}^2 + \delta_{signalShot}^2 + \delta_{BGShot}^2}} = \frac{e_s}{\sqrt{N_{DC}t_{int} + \delta_{readout}^2 + e_s + e_{BG}}} \quad (11)$$

According to Shell [23], the only noise components that need to be considered are the background shot noise and the read noise. Signal shot noise can effectively be ignored because the signal variance is not present in the background level pixels used for establishing a threshold to determine a detection event. Shell also claims that dark noise (and other noise sources) are negligible for modern dedicated detectors (assuming that temperature is kept below an appropriate threshold) with the integration times of interest. Hejduk et al. [34] also does not include signal shot noise but, unlike Shell, includes dark current noise in his calculation of the total noise. Removing signal shot noise produces the following equation for SNR:

$$SNR = \frac{e_s}{\sqrt{\delta_{dark}^2 + \delta_{readout}^2 + \delta_{BGShot}^2}} = \frac{e_s}{\sqrt{N_{DC}t_{int} + \delta_{readout}^2 + e_{BG}}} \quad (12)$$

2.6.4 Signal Photoelectrons

The SNR depends on the number of signal photoelectrons produced by the detector. Shell explains the process of calculating the number of signal photoelectrons [23]. To do this, the visual magnitude of the RSO (m_{RSO}) must be converted to absolute radiometric units to get the number of incident photons from the RSO (photons/sec/area). This conversion is done according to:

$$E_{RSO} = 5.6 \times 10^{10} \cdot 10^{-0.4 \cdot m_{RSO}} \; [ph/s/m^2] \quad (13)$$

The constant 5.6×10^{10} comes from noting that a zero-magnitude source provides an irradiance of 1.78×10^{-8} W/m^2 and that the resultant conversion from [W/m^2] to [ph/s/m^2] is done by multiplying by $\frac{\lambda}{hc}$, where λ is the wavelength of light (625 nm was

used in this case), h is Planck's constant and c is the speed of light. The incident photon flux is then converted into signal photoelectrons (e_s).

$$e_s = \eta \cdot \tau \cdot A \cdot E_{RSO} \cdot t_{sig}\ [photoelectrons] \quad (14)$$

In the above equation η is an efficiency term, τ is the finite optical transmittance loss, A is the aperture area, E_{RSO} is the photon flux, and t_{sig} is the signal integration time (not necessarily the same as the image integration time, due to the movement from the RSO from one pixel to the next). The efficiency term, η, is a combination of the quantum efficiency of the detector and the "spectral efficiency" of the detector. The spectral efficiency is the ratio of the irradiance from the spectral band of the detector to the irradiance from the entire solar spectrum. The efficiency term is simply the product of the quantum efficiency and the spectral efficiency. Two assumptions are noted by Shell for these calculations: first, for ground-based sensors there is an atmospheric loss that must be factored in but that can be ignored for space-based sensing; and second, the RSO is assumed to be a point source and all of its energy from the point spread function falls within a single pixel of the detector (meaning that a spatially extended object does not need to be considered which simplifies the SNR calculations).

2.6.5 Background Photoelectrons

The SNR also depends on the number of background photoelectrons produced by the detector. Shell also explains how to calculate the number of background photoelectrons produced for a given surface brightness of sky background (S_b) [23], which represents the visual magnitude of 1 arcsec^2 of sky. The conversion to absolute radiometric units is done similarly to above but with a conversion from arcsec^2 to steradians.

$$L_b = 5.6 \times 10^{10} \cdot 10^{-0.4 S_b} \cdot \left(\frac{180}{\pi}\right)^2 \cdot 3600^2 \; [ph/s/m^2/sr] \quad (15)$$

The background photoelectrons produced as a factor of background sky surface brightness (though slightly simplified) then is:

$$e_{BG} = \eta \cdot \tau \cdot L_b \cdot A \cdot \mu^2 \cdot t \; [photoelectrons] \quad (16)$$

The system integration time is given by t, while the instantaneous field of view of a single pixel on the detector, μ, is equal to the individual pixel size divided by the focal length of the sensor.

2.7 Star Trackers

Star trackers have become a popular sensor for determining the attitude of a satellite. There are a number of different sensors that could be used for attitude determination (sun sensor, magnetometer, gyro rate sensor, horizon sensor and star tracker); however, the star tracker is by far the most accurate (accurate down to 0.0028 degrees). A star tracker is simply a camera. It has a lens, a detector (CMOS or CCD) and an electronic unit. To determine the satellite's attitude, the star tracker takes an image of the sky. The stars in the image are compared with an onboard catalogue of stars to identify them and obtain their coordinates. The attitude of the satellite can be determined based on the coordinates of the stars in the image and their positions within the image [32].

There are many different sources of noise for star trackers. The noise sources considered in this study are dark current noise, shot noise and readout noise. These noise sources are described in Section 2.6.1 above.

Generally, star trackers avoid long exposures because long exposures raise the noise floor which is not good when detecting faint stars [35]. Typical exposure times for

star trackers are between 0.1 seconds and 1 second though some are as low as 0.01 seconds [32]. This can be confirmed by doing a survey of star trackers on the market today (see Appendix B: Survey of Star Trackers). These exposure times are comparable to those used by some dedicated space-based RSO detection sensors (Sapphire, SBV and likely HEOSS though actual exposure times for HEOSS are not known).

The field of view of a star tracker can vary anywhere between 1 degree and 20 degrees [32] although a survey of star trackers on the market today shows that most are between 10 degrees and 20 degrees (see Appendix B: Survey of Star Trackers). These fields of view are generally larger than the fields of view used by NEOSSAT, Sapphire and SBV (dedicated space-based RSO detection/tracking sensors).

Star trackers generally have sun exclusion angles between 25 and 35 degrees. Depending on baffling, however, this angle could be reduced to between 15 and 19 degrees. Typical Earth exclusion angles for star trackers are between 15 and 20 degrees and in general, most star trackers do not experience any degradation in performance with a full moon in the field of view [36]–[41].

An important consideration with star trackers that relates to RSO detection is the limiting magnitude of the camera. In terms of attitude determination, the limiting magnitude affects the field of view. To determine attitude, you need at least 3 stars visible. So, the smaller your limiting magnitude, the wider the field of view will need to be to ensure at least three stars are visible. As a point of reference, if the limiting magnitude of a star tracker is 4, then approximately 500 stars are visible to the camera [27]. According to Zakharov [32], the limiting magnitude of a star tracker varies from

approximately 5 to 11.5 depending on its purpose (high-precision, etc.). Both limiting magnitude and field of view are important factors when detecting RSOs. The larger the limiting magnitude of a sensor, the fainter an RSO can be and still be detected. When operating in stare mode, the wider the field of view of a sensor, the more likely an RSO is to pass through your field of view, increasing the likelihood of detecting RSOs. The pixel size of a CCD or CMOS star camera also affects the limiting magnitude of the camera. A larger pixel means that fewer incident electrons are needed to produce the same SNR of a smaller pixel. The smaller requirement for incident electrons increases the likelihood of faint objects being detected above the noise. So, a larger pixel size increases the limiting magnitude of the camera [35].

A star tracker would not be as efficient at observing RSOs as any ground or space based optical sensor. The sensitivity of a star tracker, which typically ranges from magnitude 5 to 11.5, pales in comparison to the dedicated sensors being used by the SSN (magnitude 15 for Sapphire, 16.5 for SBSS, 17.5 for GEODSS and 19.5 for SST). As mentioned earlier, there are two possibilities for a star tracker when it comes to RSO detection, a dual purposed star tracker and a dedicated star tracker. A dual purposed star tracker spends some of its time in RSO detection mode and some of its time in attitude determination mode. A dedicated star tracker would only operate in RSO detection mode. If the star tracker is dual purposed or it is dedicated but not the primary sensor then it would have to be operated in stare mode and not track mode. Being forced to operate in stare mode as a secondary payload would likely reduce the number of observations possible for the sensor because the star tracker may be forced to be in

a less than ideal orientation and just have to hope that RSOs will pass through its field of view (rather than slewing directly to an RSO).

Despite the disadvantage of having a lower sensitivity, there may still be an advantage to using star trackers to detect RSOs. Table 2 compares some of the specific sensors described above. The table helps assess the relative value of the different systems, particularly the cost per observation of each system. The cost of acquiring, operating and maintaining the system had to be estimated. A general rule that the annual maintenance and operation costs were 5% to 10% of the cost to acquire the system was used [12]. Using these estimates (and estimates of the number of observations per day), a cost per observation parameter could be found. The sensitivity of the systems is also shown in the table. The cost of star trackers can vary. It is difficult to find the cost of star trackers, but some have been found to range between US$30,000 and US$140,000 [36], [42]–[44]. If a star tracker were being used a secondary payload and not the primary mission, then the only cost associated with that portion of the mission would be the cost of the star tracker. Using the same rule as above (an annual cost of 10% of the acquisition cost), the annual cost of star trackers as a dedicated, secondary payload would be US$14,000. This value was used to calculate the cost per observation for a “cheap” star tracker. An “expensive” estimate for the cost of a star tracker is also provided in the table. A worst-case scenario of US$1,000,000 was used for the “expensive” case. This expensive case was obtained by increasing the cost of the most expensive star tracker that could be found (US$140,000) by an order of magnitude. Increasing the cost by an order of magnitude is intended to

account for any unknown costs (cost of launch etc.) and provide a more conservative estimate.

Table 2: Cost, latency and sensitivity comparison of RSO detection systems

System	Observations per Day	Cost per Observation	Sensitivity (magnitude)
GEODSS Network [12]	113,400	$0.76	17.5
SST [12]	25,200	$1.59	19.5
Sapphire [12]	1,600	$21.92	15.0
SBSS [12]	12,000	$23.05	16.5
Cheap* Star Tracker	1	$38.34	5 – 11.5
Cheap* Star Tracker	10	$3.84	5 – 11.5
Cheap* Star Tracker	100	$0.38	5 – 11.5
Expensive** Star Tracker	1	$273.97	5 – 11.5
Expensive** Star Tracker	10	$27.39	5 – 11.5
Expensive** Star Tracker	100	$2.74	5 – 11.5

* Cheap refers to a star tracker with an annual cost of US$14,000 (10% of $140,000)
** Expensive refers to a star tracker with an annual cost of US$100,000 (10% of $1,000,000)

The lower sensitivity of star trackers compared to dedicated sensors does not necessarily disqualify them from being used for RSO detection. Even with an expensive star tracker, the cost per observation can drop to just a little bit more expensive than other space-based sensors with as few as ten detections per day. With 100 detections per day, the cost per observation can drop to just above that of ground-based sensors, an order of magnitude lower than Sapphire and SBSS. If these detection rates are possible then star trackers may be a very low-cost addition to the efforts already being made to detect RSOs. Due to their low cost, there is also the potential to fill some of the gaps in coverage that both ground and space-based sensors have. Multiple star

trackers could be put in to various orbits as secondary payloads to fill the gaps that SBSS, Sapphire and the few other space-based RSO detection systems have at a fraction of the cost. A “hole” in coverage could potentially be plugged by a star tracker placed in a specific orbit at a much-reduced cost than a dedicated ground or space-based system. What star trackers lack in performance they would make up for in low cost and versatility.

Some work in the area of using star trackers for RSO detection has already been done. In November of 2017, researchers from the Sapienza University of Rome and ARCA Dynamics proposed a mission architecture called ROMULUS (Recognition of Orbiting-objects through optical MeasUrements of Light-reflecting-targets by Using Star-sensors) [45]. This architecture is similar to what is being proposed in this thesis but is more specific. ROMULUS is identified as a secondary payload that gets optical data from an inactive star tracker. The ROMULUS architecture assumes that there are three star trackers available on the host satellite. With three star trackers, ROMULUS can minimize its effect on the satellite and its primary mission. Three operation modes are identified for this architecture:

1) One of the star trackers that is not being used for attitude determination is chosen for ROMULUS. The FOV orientation depends on the orientation required by the primary mission.
2) The star tracker that has the best orientation for RSO detection is selected for ROMULUS even if that star tracker could be used for attitude determination, as long as there is a still a star tracker that can be used for attitude determination (though less optimal for attitude determination).

3) The satellite orientation is changed to give the star tracker chosen for ROMULUS the best viewing conditions possible.

There are three different components to the ROMULUS architecture: the star tracker that collects the data, on-orbit processing software and processing software for use on the ground. The on-orbit processing software would obtain the extremal points of an RSO streak (the beginning and end of a streak). That information would then be sent to the ground and processed to determine the orbit of the RSO and update the catalogue.

As well as proposing the ROMULUS architecture, Curti et al. [45] also performed a feasibility study. They simulated two Sun-synchronous satellites with an altitude of approximately 650 km. They simulated Ram and anti-Sun orientations and imposed a number of constraints on the requirements for detecting an RSO. From their results they noted that the best detection rate possible (for the given scenarios) was one detection every two minutes, which translates to approximately 730 detections per day. The proposed ROMULUS architecture has the same objective as this thesis, improving the current state of space situational awareness. If similar detection rates from this work can be reported, then the confidence in the use of star trackers will be stronger than what can be given by a single study.

Work has also been done on the image processing side of RSO detection, which is outside of the scope of this thesis. Karl Bernander examined several different RSO detection algorithms and how to obtain the orbit of the RSO after detecting it [46]. To test the algorithms, he created simulated images. The images were constructed by adding stars and various noise sources (blurring, banding noise, gaussian noise and salt and pepper noise). The RSOs were then added to the images by simply including

lines (i.e., streaks) of varying length and intensity. The RSOs were not modelled based on actual RSO positions or brightness. Bernander determined which algorithms performed the best and that an imprecise preliminary orbit could be determined with three measurements that have small time differences. He was, however, unable to draw any conclusions about how technically feasible his methods were but believed that implementing this on-board would be possible.

Chapter 3: Analytic Simulator Description

The purpose of the Analytic Simulator is to estimate the detection rate of a star tracker (ST). The detection rate of a sensor is the number of RSOs detected over a given period of time. The algorithm was developed as a MATLAB function and takes several inputs. The main script of the function is composed of just under 1,000 lines of code and consists of 28 sub-functions created for this simulator (and the image simulator) along with 13 functions used to run the SGP4 propagator (Section 3.1.1 gives more detail on the propagator). The SGP4 code was compiled by Vallado et. al. [47] and can be downloaded from [48]. The inputs the simulator takes are the two-line element set (TLE) of a host satellite for the star tracker, a list of TLEs for each RSO that is to be included in the simulation, various star tracker parameters, the star tracker orientation, the start and stop times of the scenario and other variables related to the simulation. Using these inputs, the simulator propagates the orbit of the star tracker on the host satellite and determines how often (and when) an RSO crosses the field of view of the star tracker and also how often (and when) that RSO is bright enough to be considered detected.

Table 3 lists the parameters that the analytic simulator uses to define the sensor being simulated. These parameters can be varied which allows different star trackers (or other sensors) to be simulated. A list of a few different sensors and their parameters is given in Table 4.

Table 3: Overview of Analytic Simulator Parameters

Category	Parameter	Description/Comment
Optics	Aperture Diameter	Aperture diameter of the lens of the sensors.
Optics	Focal Length	Focal length of the sensor
Optics	Optical Transmittance Loss	Optical transmittance loss of the detector
Detector	Number of Pixels	Number of pixels on one edge of the detector (assuming a square detector)
Detector	Quantum Efficiency	Quantum efficiency of the detector
Detector	Pixel Dimensions	Individual pixel dimension of one edge of the pixels on the detector (assuming square dimensions)
Detector	Integration Time	Integration time of the detector
Detector	Read Noise	Read noise of the detector
Detector	Dark Current	Dark current of the detector
Detector	Spectral Range	The spectral range of the detector
Sensor	Sensor Attitude	The attitude of the sensor with respect to the host satellite is defined by three Euler angles (θ_x, θ_y, θ_z)
Sensor	Sensor Operation Length	The percentage of the scenario time that the sensor is operating in RSO detection mode
Sensor	Earth Exclusion Angle	The angle that the boresight must be away from the limb of the Earth to not have the field of view washed out by Earth glow
Sensor	Sun Exclusion Angle	The angle that the field of view must be away from the limb of the Sun to not have any direct solar light enter
RSOs	RSO Diameters	Method used to simulate the diameter for each RSO
RSOs	RSO Reflectivity	The reflectivity used to model the RSOs
Scenario	Earth's Radius	The radius of the Earth
Scenario	Host Satellite Attitude	The attitude of the host satellite is defined by three Euler angles (yaw, pitch and roll) and a coordinate system selected by the user (ECI, orbital or anti-sun)
Scenario	Start Time	The start date and time of the scenario in UTC
Scenario	Stop Time	The stop date and time of the scenario in UTC

Table 4: List of example sensor parameters

Parameter	Near Earth Space Surveillance Imager – NEOSSAT [14], [49]	Optical Imaging Subsystem – Sapphire [16], [50]	Fast Auroral Imager (FAI) (NIR) – Cassiope [51]–[54]	AD-1 Star Tracker (Mars Bureau) [32]	ST-16RT2 Star Tracker (Sinclair Interplanetary) [36], [55]–[57]	BOKZ-MF Star Tracker (IKI RAN) [58]–[61]
Aperture Diameter	15 cm	15 cm	17 mm	28.8 mm	10 mm	18 mm
Focal Length	89.3 cm	45 cm*	68.9 mm***	51.8 mm	16 mm	32 mm
Number of Pixels	1024 x 1024	1024 x 1024	256 x 256	512 x 512	2592 x 1944	512 x 512
Quantum Efficiency	78%	61%**	66%	20%	Max 45%	Max 58%
Pixel Dimensions	13 μm	13 μm	26 μm	23 μm	2.2 μm	20 μm
Integration Time	--	0.1 s and 0.4 s	0.1 s	0.5 s	--	0.25 s
Read Noise	2 e^- rms / pixel	2 e^- rms / pixel	12 e^- rms	40 e^-	3 e^-	22 e^- rms
Dark Current	20 ke^-/pixel/s at 293 K	250 e^-/pixel/s at 293 K	529 e^- /pixel/second at 293 K	3000 e^-/s at 293 K	25 e^-/pix/s at 328 K	400 e^-/pixel/s at 298 K
Spectral Range	350 – 1050 nm	300 – 900 nm	650 – 1100 nm	400 – 1000 nm	--	400 – 1000 nm
ADC Resolution	--	--	16 bits	--	12 bits	12 bits

* Based on focal ratio of f/3 used by the Space Based Visible (SBV) Sensor which has the same basic telescope architecture [62], [63].
** Worst case peak efficiency at 600 nm [50].
*** The focal length of the FAI sensor is 68.9 mm and it has a f-number of f/4. This gives it an aperture of 17 mm. However, the FAI sensor has an effective f-number of f/0.8. This gives it an effective focal length of 13.8 mm

The majority of the optics and detector parameters in Table 3 are used in the calculation of the signal-to-noise ratio and explained in Chapter 2. The focal length, number of pixels and pixel dimensions are used to determine the field of view of the sensor which is described in Section 3.1.4 below. The spectral range is used to determine the spectral efficiency of the detector, which is then used in the calculation of the signal and background electrons. The spectral efficiency is found by integrating the irradiance of the solar spectrum across the spectral range of the detector and dividing that by the irradiance of the entire solar spectrum. The sensor and host satellite attitudes define the orientation of the sensor and are explained in detail in Section 3.1.2 below. The sensor operation length defines the percentage of the scenario time that the sensor is operating in RSO detection mode. It is used to simulate dual-purposed star trackers that spend part of their time in an attitude determination and control mode and part of their time in an RSO detection mode. The sensor operation length is defined by two variables, a duration and a percentage. The duration defines the length of each RSO detection mode period, and the percentage defines the total amount of time of the entire scenario that the sensor operates in this mode. The simulator splits the scenario time into evenly distributed periods of operations in RSO detection mode. For example, if the duration was 60 seconds and the percentage was 50%, the simulator would break the scenario time in to alternating periods of operation and non-operation of the RSO detection mode. The sensor would operate in RSO detection mode for a 60 second period and then it would stop for a 60 second period (during which no RSOs could be detected). The simulation only splits the scenario time in to alternating periods of operation and non-operation. It is not able define operation periods of different lengths

in the same scenario. If the operation percentage is set to 100% then the sensor operates in RSO detection mode continuously. The Earth and Sun exclusion angles are the angles that the field of view must be away from the limb of the Earth and Sun respectively to avoid having the detector dominated by these light sources. The RSO diameters and reflectivity are used to determine the visual magnitude of the RSO as described in Equations 7 and 8.

The analytic simulator has multiple outputs. The most significant outputs are four parameters: total accesses, unique accesses, total detections and unique detections. The term “access” refers to any RSO that crosses the field of view of the star tracker while “detection” refers to an RSO that crosses the field of view of the star tracker and is above a minimum signal-to-noise detection threshold. The term “total” refers to the cumulative number of events (accesses or detections) that occur, including repeat events of the same RSO. The term “unique” refers to the number of events that occur without counting multiple events of the same RSO (i.e., detections of the same RSO multiple times counts as a single detection). The “total” number describes how much a particular star tracker contributes to updating the positions of RSOs for a catalog. The “unique” number indicates what percentage of RSOs is updated in the catalogue. There is a difference in value in detecting the same object one hundred times in a day or detecting twenty different objects five times each in a day (though each case has one hundred total detections). The other outputs of the simulator are the length of time required to run the simulation (and the length of time required to simulate each individual RSO), as well as two different structures that are used to produce images

based on the simulation. More details on the image simulator are described in Chapter 4.

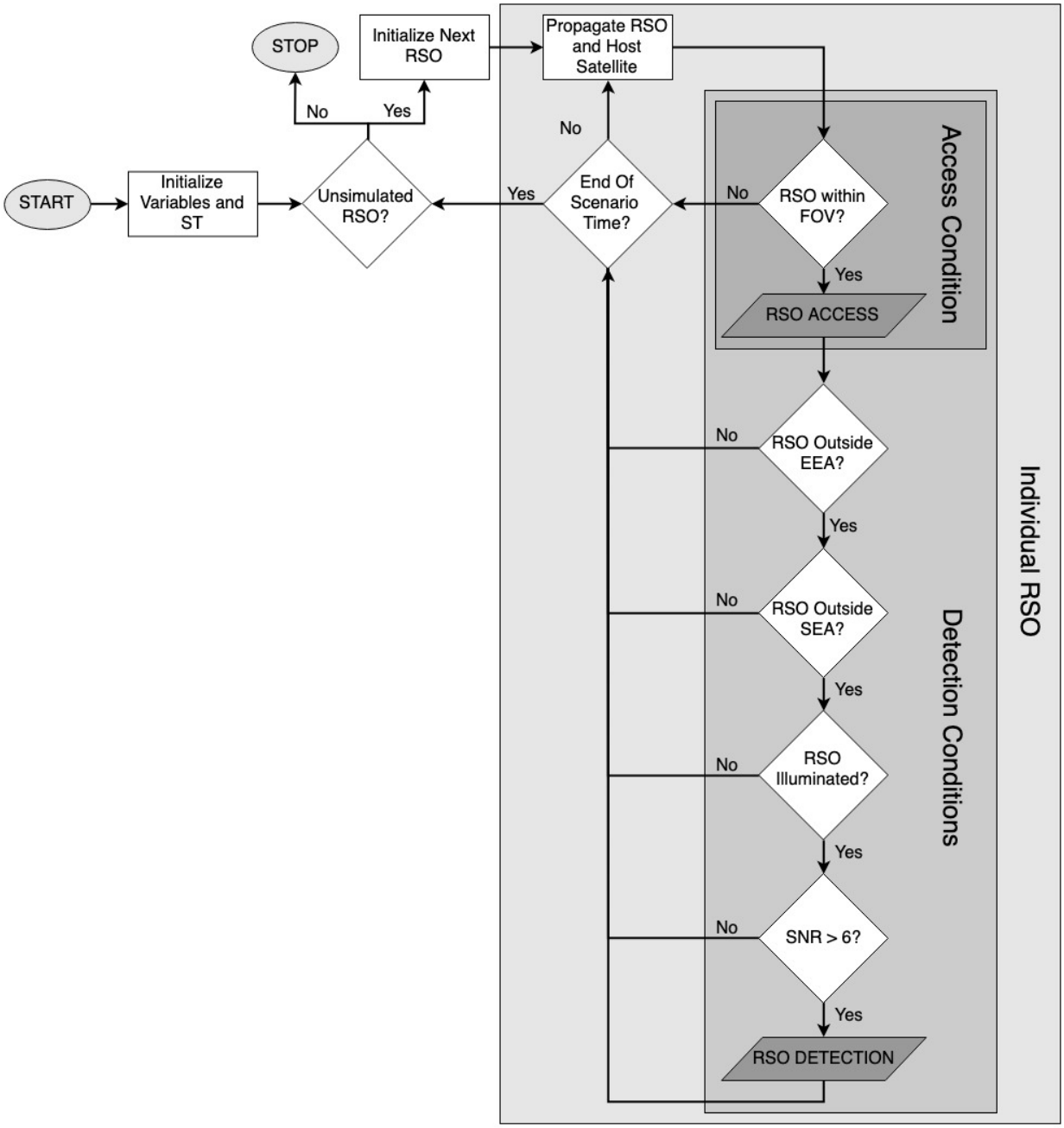

Figure 5: Block diagram of analytic simulator

The simulator runs through each individual RSO one at a time. It determines all of the access and detection times for a single RSO for the entire scenario and then moves on to the next RSO. This allows the simulator to use a variable step size when

propagating the orbits of the star tracker and RSOs. When the RSO of interest is far away from the field of view a large step size can be used which helps reduce the runtime of the simulator. Reducing the run time by varying the step size would not be possible if all of the RSOs were simulated together instead of individually.

The simulator begins by determining whether or not the RSO falls within the field of view of the star tracker. If the RSO falls within the field of view (and is not hidden behind the Earth) then the RSO is considered accessed. If the RSO is accessed, then the next step is to determine if the RSO can be detected. For an RSO to be detected (1) the boresight of the sensor must be outside the Earth exclusion angle (EEA), (2) the boresight must be outside the Sun exclusion angle (SEA), (3) the RSO must be illuminated by the sun and not in eclipse and (4) the RSO must have an SNR greater than or equal to 6. If all of the above conditions are met, then the RSO is considered detected. A block diagram of the simulator showing the major components of the access and detection algorithm is shown in Figure 5 above.

3.1 Technical Considerations of the Analytic Simulator

Below is a description of some of the major technical aspects of the analytic simulator and how it operates. Resident space object propagation, host satellite and sensor attitude, RSO diameter estimation, sensor field of view and the SNR threshold are all discussed.

3.1.1 Resident Space Object (RSO) Propagation

As discussed in Chapter 2, the U.S. maintains a catalogue of objects tracked by the Space Surveillance Network at space-track.org. The catalogue has both current and past two-line element sets (TLEs) for the RSOs that the SSN tracks. These TLEs can

be downloaded in bulk and saved as text files. The analytic simulator takes these TLEs and uses them to define each of the RSOs to be included in the simulation. Only RSOs that have TLEs provided to the simulator will be considered in the simulator. Providing only desired TLEs allows different portions of the RSO population to be simulated while ignoring other portions, helping to prevent detection rates from being "polluted" with RSOs that are not of interest. For example, GEO satellites could be simulated to determine a sensor's impact on the cataloguing of this class of satellite. A limitation of using TLEs is that only an RSO that has previously been catalogued can be simulated. If the RSO has never been detected, and by extension does not have a TLE, it cannot be included in the simulation. The simulator cannot "discover" any new satellites. A second limitation is that for the simulation to be accurate, the RSO must have a TLE that has been generated around the same time as the desired scenario interval (within a few days [64]). If the scenario interval of the simulation is off by more than a few days, the accuracy of the TLE and its ability to be used for propagation quickly begins to drop. This decrease in accuracy means that an RSO can only be simulated if it has been observed and had its TLE updated within days of the desired simulation period. This also means that an entire new set of TLEs must be obtained for each different scenario that is to be simulated that differs by more than a few days, which can be time consuming.

To determine the position of the RSOs (and the host satellite) at different times, a propagator is needed. The basic equations for orbital motion assume that the Earth is spherical and that no other forces act on the orbiting body other than the gravitational force from the Earth. The Earth, however, is not spherical but is flattened at the poles

and bulges at the equator. This asymmetric distribution of mass causes the acceleration of an RSO to be more complicated than that caused by a perfectly spherical Earth [65]. An RSO also experiences gravitational forces from the Sun and the Moon, not just the Earth. Earth's oblateness, the Sun and the Moon are all sources of additional forces that cause the orbit of an RSO to drift over time [65]. An RSO also experiences atmospheric drag which acts in the direction opposite to the RSO's motion causing it to lose energy and its orbit to become smaller [65]. Ignoring these phenomena make the basic equations for orbital motion inaccurate. To propagate the positions of the RSOs (and the host satellite), the simulator uses an SGP4 propagator. The SGP4 propagator is used for near-Earth satellites (satellites with periods less than 225 minutes) [66] and predicts the position and velocity of a satellite while taking in to consideration both the secular (linear) and periodic variations caused by Earth's oblateness, solar and lunar gravitational effects, gravitational resonance effects and drag [67]. A detailed explanation of the SGP4 code that was used by the simulator can be found in *Revisiting Spacetrack Report #3* by Vallado et al. [47] and additional information can also be found in *Spacetrack Report No. 3* by Hoots and Roehrich [66].

3.1.2 Host Satellite and Sensor Attitude Definition

The simulator operates in stare-mode and is not designed to operate in track-mode. The host satellite is fixed with respect to the coordinate system used to define its attitude. It is not time variable. Being fixed in the defining coordinate system does not necessarily mean that the host satellite's attitude is inertially fixed. If the coordinate system used to define the attitude of the host satellite is inertial then the satellite's attitude is inertially fixed. If, however, a non-inertial coordinate system is used to define

the host satellites attitude (such as the orbital system described below) then the attitude of the host satellite is non-inertial as well.

To define the attitude of the host satellite the user defines the yaw, pitch and roll angles, as well as the coordinate system in which the rotations are referenced too. Rotations are performed in the following order: roll, pitch and yaw. All rotations follow the right-hand rule when rotating about a given axes. If the yaw, pitch and roll angles were all zero then the X, Y and Z axes of the spacecraft would be perfectly aligned with the X, Y and Z axes of the selected coordinate system. There are three coordinate systems used in the simulator: the Earth-Centred Inertial (ECI) frame, the orbital frame and the anti-sun frame. The ECI frame is centred on the Earth with the X-axis pointing to the Vernal Equinox, Z-axis pointing to the celestial north pole and the Y-axis completing the right-handed system (RHS). All axes are referenced to the J2000 epoch. The orbital frame is centred on the spacecraft with the Z-axis pointing Nadir, the Y-axis pointing in the negative orbit normal direction and the X-axis completing the RHS. The anti-sun frame is centred on the Earth with the X-axis pointing in the negative Earth-Sun direction, the Z-axis pointing to the ecliptic normal (the J2000 ecliptic normal) and the Y-axis completing the RHS.

The sensor is fixed in a given orientation for the entire simulation scenario with respect to the host satellite. Sensor attitude is defined by three angles (θ_x, θ_y and θ_z) relative to the spacecraft frame. It is obtained by rotating in the order θ_z, θ_y, θ_x. The default sensor orientation ($\theta_x/\theta_y/\theta_z$=0º/0º/0º) is along the X-axis of the spacecraft. All rotations follow the right-hand rule when rotating about a given axes.

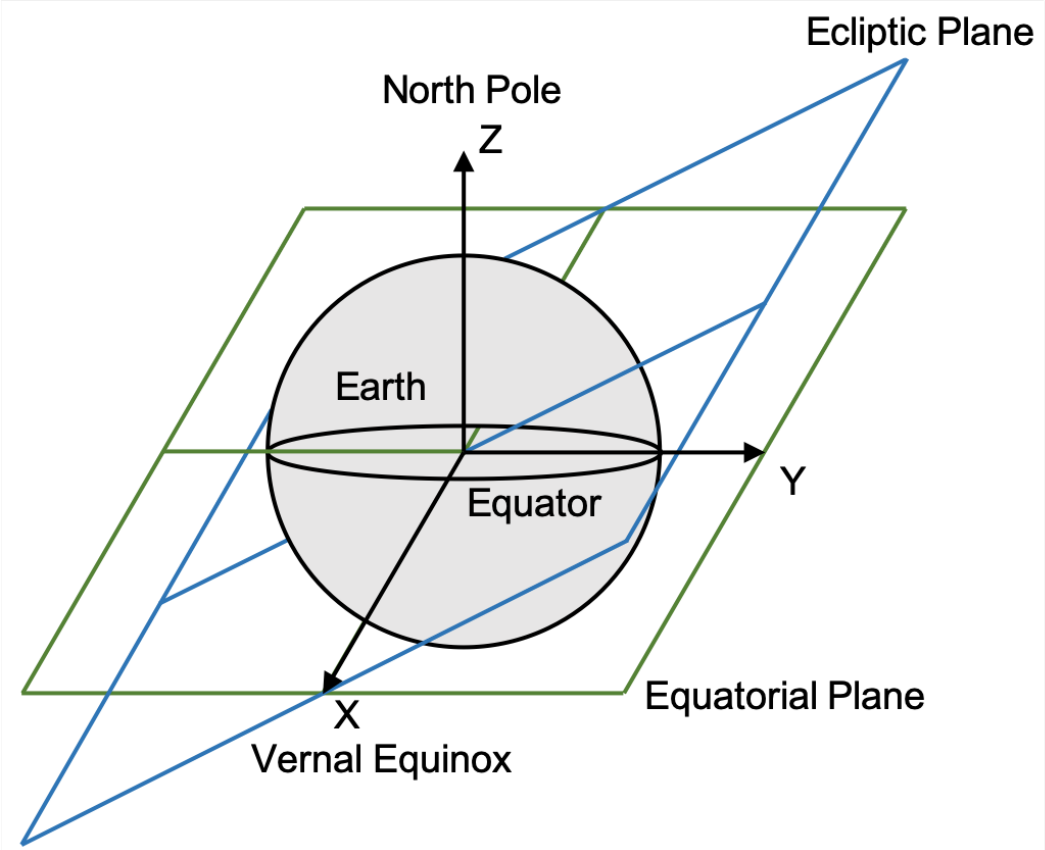

Figure 6: Earth-Centred Inertial (ECI) Coordinate System

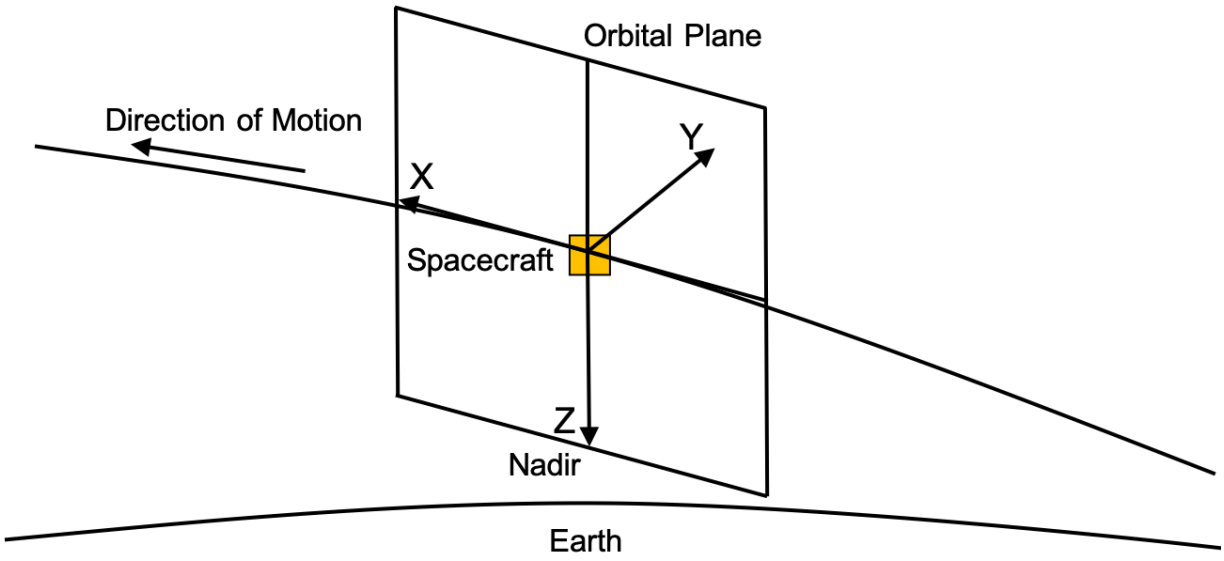

Figure 7: Orbital Coordinate System

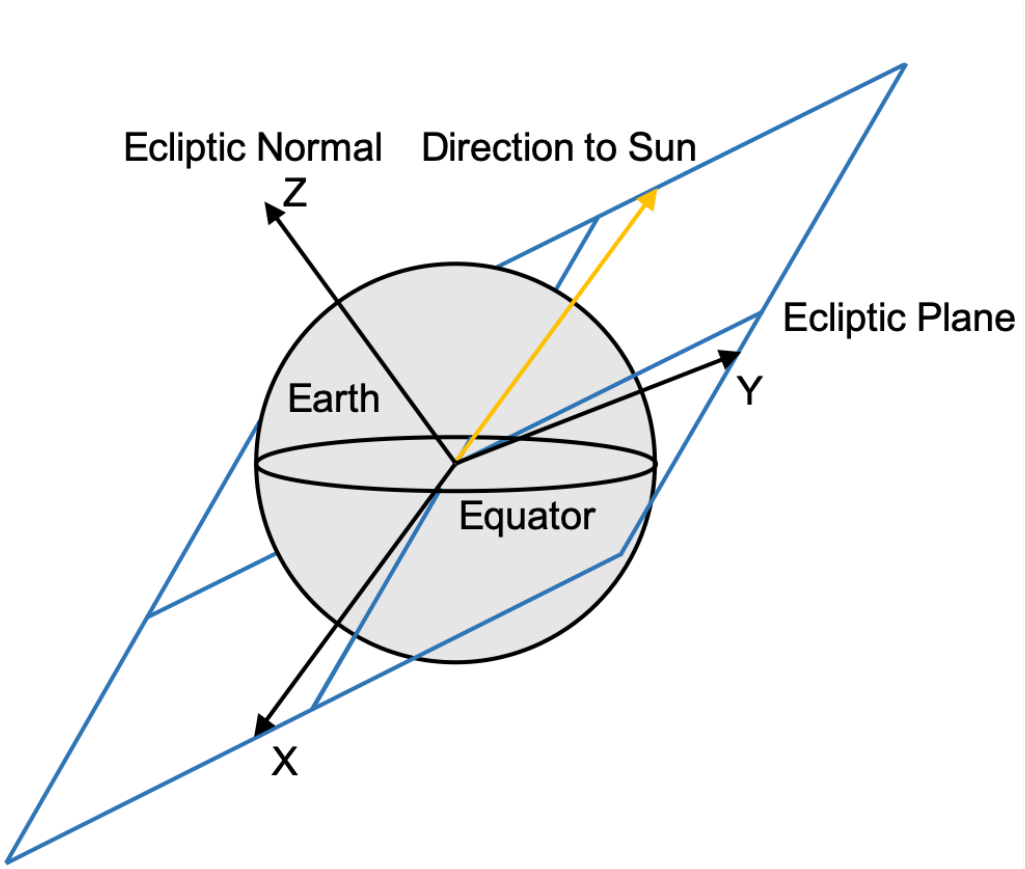

Figure 8: Anti-Sun Coordinate System

Figure 9 shows how the reference coordinate system, host satellite coordinate system and sensor coordinate system relate to each other. In this example, the orbital coordinate system is used as the reference frame. The spacecraft attitude is defined relative to this frame. The top left portion of the figure shows the attitude of the spacecraft. The spacecraft coordinate system has been rotated about the orbital Z-axis by 180 degrees (yaw/pitch/roll = 180°/0°/0°) which defines the host satellite's attitude. The top right portion of the figure shows the sensor's orientation with respect to the host satellite. The sensor has been rotated 45 degrees about the spacecraft's Y-axis ($\theta_x/\theta_y/\theta_z$=0°/45°/0°). This defines the sensor's attitude. The sensor's field of view is also shown in orange pointing along the sensors X-axis. The bottom portion of the figure shows all three coordinate systems (reference, host satellite and sensor) all together.

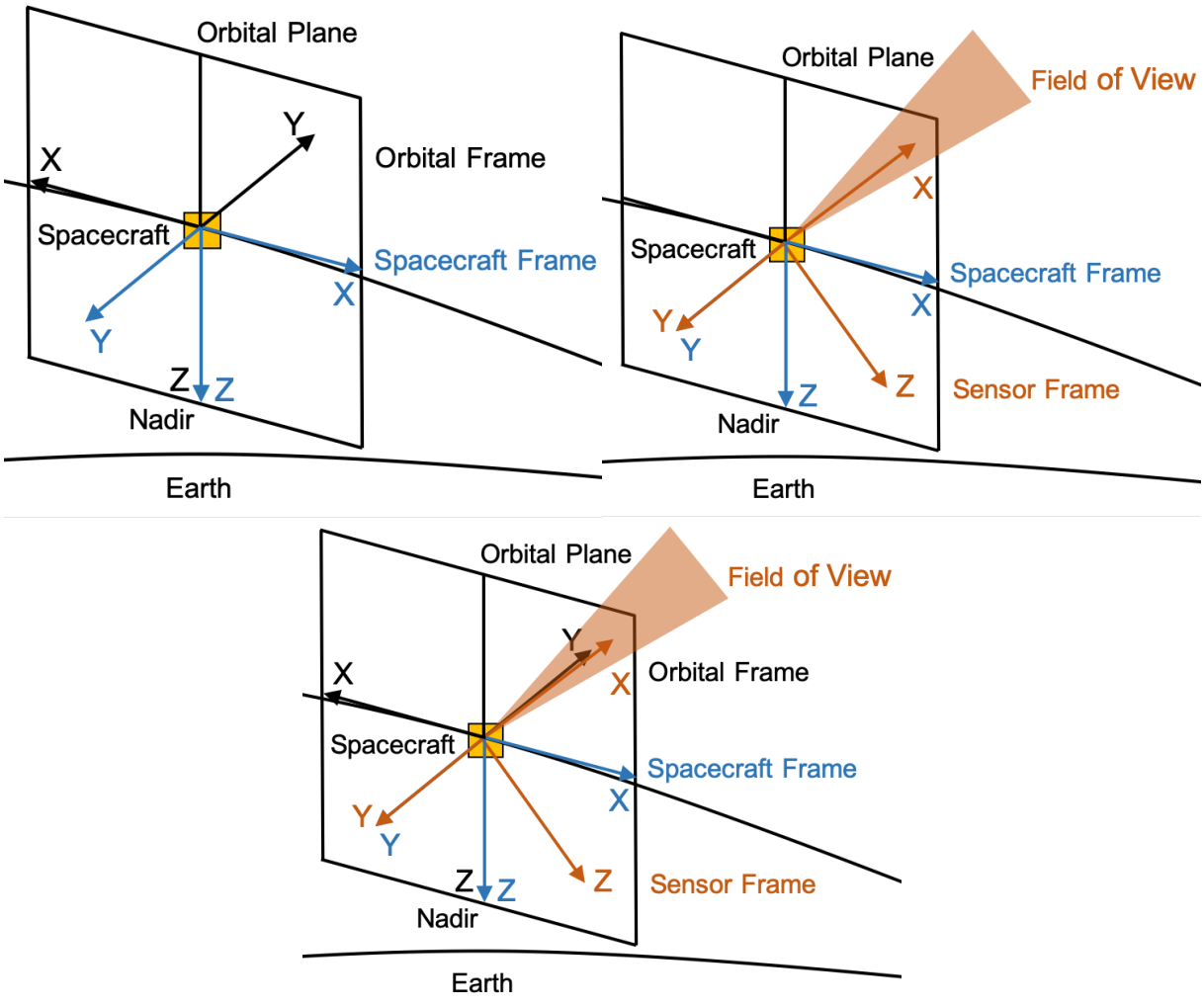

Figure 9: Example of Host Satellite and Sensor Attitude Definition. (Top Left) Reference coordinate system (Orbital) and spacecraft coordinate system. (Top Right) Spacecraft coordinate system and sensor coordinate system. (Bottom) All three coordinate systems. Note sensor field of view shown in orange pointing along sensor x-axis.

3.1.3 RSO Diameter Estimation

To determine whether an RSO is detectable by a star tracker, the size of the RSO must be known. TLEs and space-track.org do not provide the physical sizes of the RSOs. Because of this, the size of each RSO has to be estimated. RSOs are assumed to be spheres and therefore the only dimension to estimate is the diameter of the RSO.

The analytic simulator has three different approaches to assigning an RSO an absolute diameter that can be used depending on the purpose of the simulations:

a) A fixed diameter of 10 cm
b) A combined distribution of different types of RSOs
c) A user defined diameter assigned to all RSOs (requested as user input by the simulator during runtime)

Method a) is included to provide a worst-case scenario by simply assigning each RSO the smallest possible diameter for an object tracked by the SSN. Method b) attempts to reflect the size distribution in the RSO catalogue most accurately. There are three main types of RSOs recorded in the catalogue: debris, rocket bodies and payloads (active and inactive satellites). Normal distributions for the different types of RSOs contained within the catalogue are combined in to a single distribution from which RSO diameters are assigned. Each type of RSO has its own mean, standard deviation and weight. The weights were assigned according to the percentage of the population that the type of RSO makes up. Debris make up 64% of the space catalogue so the weight used for that distribution is 0.64. Rocket bodies likewise make up 11% of the catalogue and payloads 25%, so their weights were 0.11 and 0.25, respectively.

Table 5: Statistics used to model RSO diameters based on RSO types

RSO Type	Mean	Variance	Weight
Debris	10 cm	50 cm	0.64
Rocket Body	5 m	1 m	0.11
Payload	1 m	1 m	0.25

Figure 10 shows a histogram of the distribution of 100 000 diameters produced by this method of combining normal distributions for different RSO types. The figure shows that the majority of generated diameters are below one metre in diameter

(representative of the debris and payload population) with a small number of RSOs with larger diameters around 5 m (representative of rocket bodies).

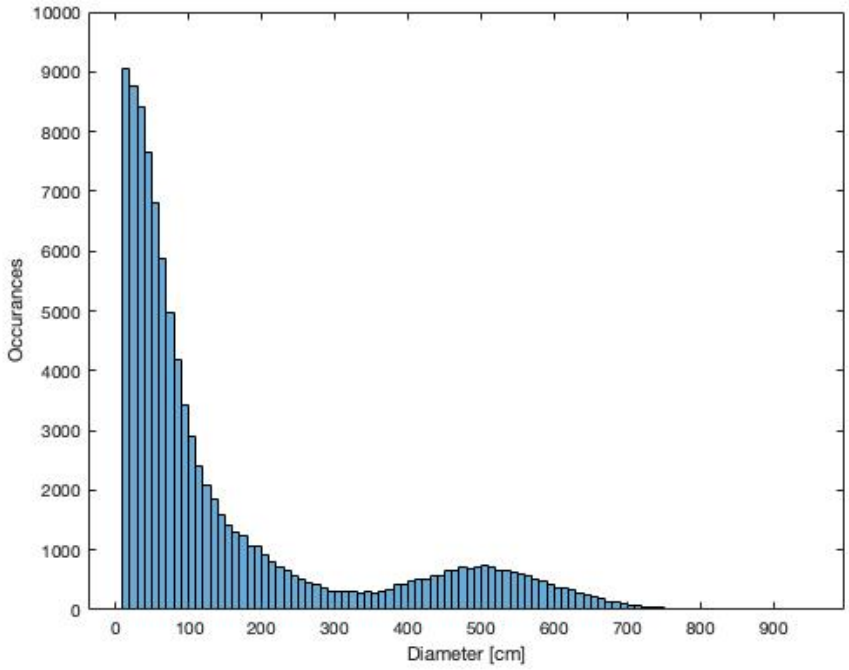

Figure 10: Histogram of 100 000 generated RSO diameters

Method c) is simply a user defined diameter in which every RSO is assigned the same diameter which is selected by the user. It is useful for the simulation of a single RSO with a known size but less helpful when doing bulk catalog simulations.

Methods a) and c) are for special cases (worst case scenarios or single RSO simulations etc.). Method b) is used for bulk catalog simulations. Unless otherwise stated, method b) was used to simulate the diameters of RSOs for the results presented in this thesis.

3.1.4 Sensor Field of View

The analytic simulator treats the sensor as having a conic field of view as opposed to a rectangular field of view. When talking about the field of view of a sensor, the half-conic angle is used to describe the size of the field of view. The field of view of

the sensor is not directly defined by the user. Rather, it is derived based off of other user-defined sensor parameters as shown below: the number of pixels on one side of the detector (n) (assuming a square detector), the size of one side of an individual pixel (x) (assuming a square pixel) and the focal length of the sensor (f).

$$FOV = \frac{nx}{2f} \tag{17}$$

3.1.5 Signal-to-Noise Threshold

The default threshold for identifying when an RSO is detected is an SNR of 6. Shell [23] suggests an SNR of 6 to keep false alarms at a minimum. Hejduk et al. [34] identifies a SNR threshold of 8 for a sensor operating in track mode and a SNR threshold of 3 for a sensor operating in sidereal mode (as the simulator is). Hejduk claims that in sidereal mode, the RSO will produce a streak across multiple pixels and that because of this, a smaller threshold is required to identify the RSO. An SNR threshold of 6 is a more conservative threshold than the one proposed by Hejduk and is therefore selected.

3.2 Analytic Simulator Validation

To validate the accuracy of the analytic simulator and its results, the access times determined by the simulator were compared with access times determined by Systems Tool Kit (STK), a software produced by Analytic Graphics, Inc. (AGI) for satellite analysis. The test was run for a full year period with a single RSO. Both the simulator and STK (using an SGP4 propagator) were run with the same host satellite and RSO TLEs. All of the start of access (SOA) times, end of access (EOA) times and duration of access (DOA) times were recorded for both the simulator and STK. The recorded times were then compared.

Figure 11 shows three plots of the error in start, end and duration times. The maximum error in start or stop time was one second. A positive error means that the simulator start/end time occurred after the STK start/end time. A negative error means that the simulator start/end time occurred before the STK start/end time. A negative duration means that the simulator duration was shorter than the STK duration. All of the start times have positive errors meaning that the simulator consistently accessed the RSO right after STK did. All of the end times have negative errors meaning that the simulator consistently ended access times right before STK did. This would result in the simulator consistently having shorter access durations than the simulator which is what we see in the third graph in Figure 11, consistent negative durations.

In total there were 712 accesses during the test for both the simulator and STK which means that the simulator did not miss any of the accesses that occurred. The RMS error for the start, end and duration of each access was calculated. Both the start and end times had an error of approximately half a second and the total duration had an error of one second. The average DOA time was approximately 83 seconds. An error of one second is acceptable considering most durations were significantly longer than that.

This test shows that the simulator is accurately calculating the access times for a sensor and an RSO. It is correctly propagating the orbits and determining when an RSO is within the field of view of the sensor with an accuracy of one second.

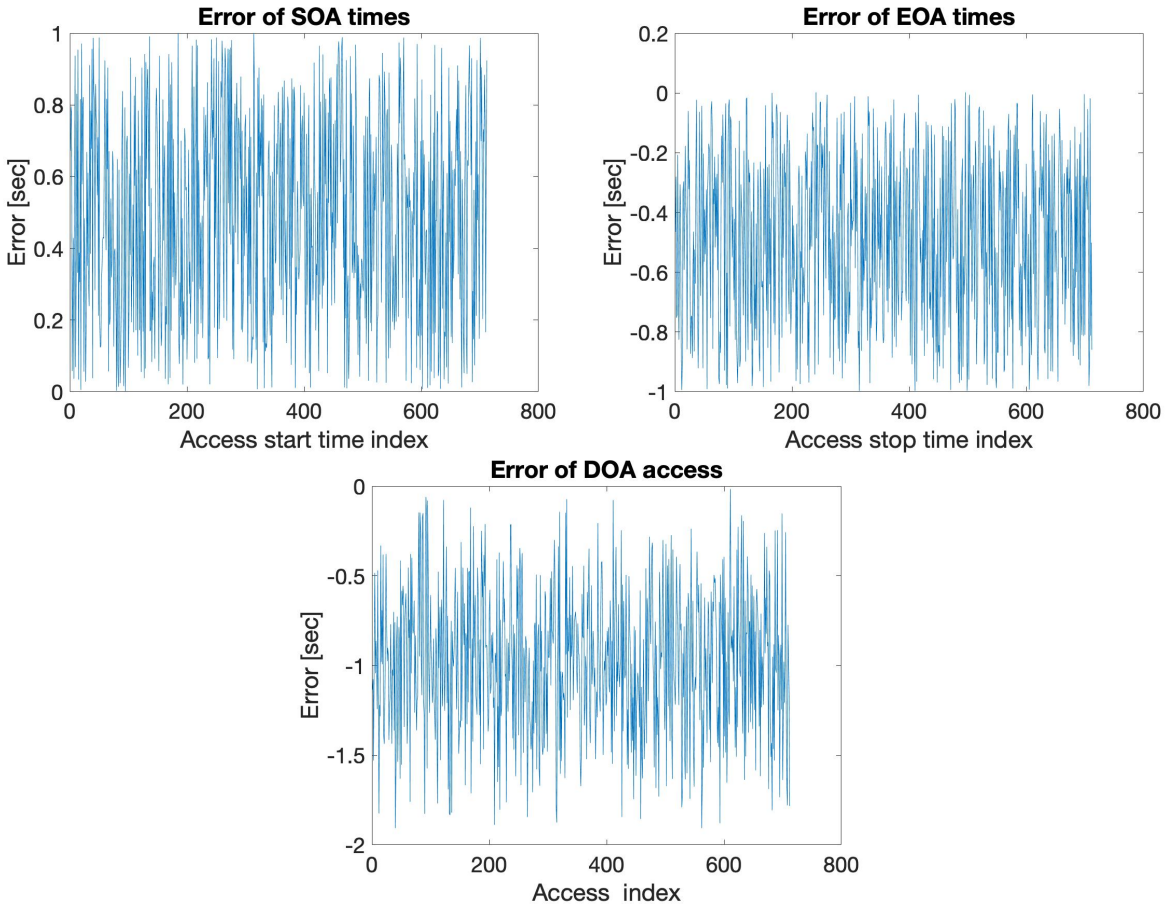

Figure 11: Error in access times

Table 6: RMS error in SOA, EOA, DOA times

	RMS Error
Start of Access	0.568 [sec]
End of Access	0.563 [sec]
Duration of Access	1.060 [sec]

Table 7: Minimum, maximum and average DOA times

	Duration of Access	
	Simulator	**STK**
Minimum	5 [sec]	6.1 [sec]
Maximum	109 [sec]	109.3 [sec]
Average	82.9 [sec]	83.9 [sec]

To validate the accuracy of the detections being recorded by the simulator, the visual magnitude of all the accessed and detected RSOs for a sample scenario was

examined. The visual magnitude of RSOs is discussed in Section 2.5 The analytic simulator should only detect objects that are within the limiting magnitude of the sensor. To ensure that the simulator is only detecting objects within this magnitude, the simulator was run three times. Each time the simulator was run the RSOs were given a diameter of 0.1 m, 1 m and 10 m, respectively. Each of the accesses and detections were then plotted on a visual magnitude versus distance plot. The scenario was run using the Fast Auroral Imager (FAI). The FAI sensor is on board the Cassiope satellite as part of the ePOP (Enhance Polar Outflow Probe) science mission. The purpose of FAI is to measure large-scale auroral emissions. It measures these auroral emissions with the near-infrared wavelengths (650 nm – 1100 nm) and a monochromatic wavelength of 630 nm. The parameters for FAI are shown in Table 8. Images from FAI are publicly available from the ePOP website [68]. Because the images are easily accessible, as opposed to images from COTS star trackers which are not readily available, they were used to validate different portions of the analytic and image simulator. For this reason, the FAI sensor was used here to validate the detections made by the analytic simulator as well. Instead of using Cassiope as the host satellite, Sapphire was used. Sapphire was used because it gets closer to some RSOs than Cassiope providing a greater range of data to analyze.

To test whether the detections being recorded by the simulator were within the limiting magnitude of the FAI, the limiting magnitude had to first be determined. The limiting magnitude of a sensor can be determined by using the SNR Equations 12-16 described earlier. These equations can be rearranged to solve for the visual magnitude,

m_{RSO}. If the SNR threshold is used, then m_{RSO} becomes the limiting magnitude of the sensor and can be determined as shown below.

$$m_{lim} = -2.5\, log\left[\frac{SNR\sqrt{\delta_{dark}^2 + \delta_{readout}^2 + \delta_{BGShot}^2}}{QE \cdot \tau \cdot A \cdot 5.6 \times 10^{10} \cdot t_{sig}}\right] \quad (18)$$

The FAI parameters are given in Table 8. Using Equation 18 (assuming a SNR threshold of 6 and background of 22 mv/arcsec^2, an estimate for the sky background as described earlier), the limiting magnitude of the FAI sensor was determined to be 8.7. Note that the equation for the limiting magnitude of a sensor is ideal in the sense that it assumes the object being imaged is not moving relative to the sensor.

Table 8: FAI parameters [51]–[54]

Parameter	**Value**
Pixels	256 x 256
Quantum Efficiency, QE	0.66
Optical Transmittance Loss, τ	0.9
Aperture Diameter	1.7 cm*
Pixel Size	26 μm
Effective Focal Length	1.38 cm*
Integration Time	0.1 seconds
Read Noise	12 RMS e^-
Dark Current	529 e^-/pixel/second

* The focal length of the FAI sensor is 68.9 mm and it has a f-number of f/4. This gives it an aperture of 17 mm. However, the FAI sensor has an effective f-number of f/0.8 which gives it an effective focal length of 13.8 mm.

In the figure below the three different RSO sizes are clearly distinguishable. Accesses are shown as the blue circles and detections are shown as the red dots. An RSO that was accessed is represented as a blue circle. An RSO that was accessed and detected is represented as a blue circle with a red dot in it.

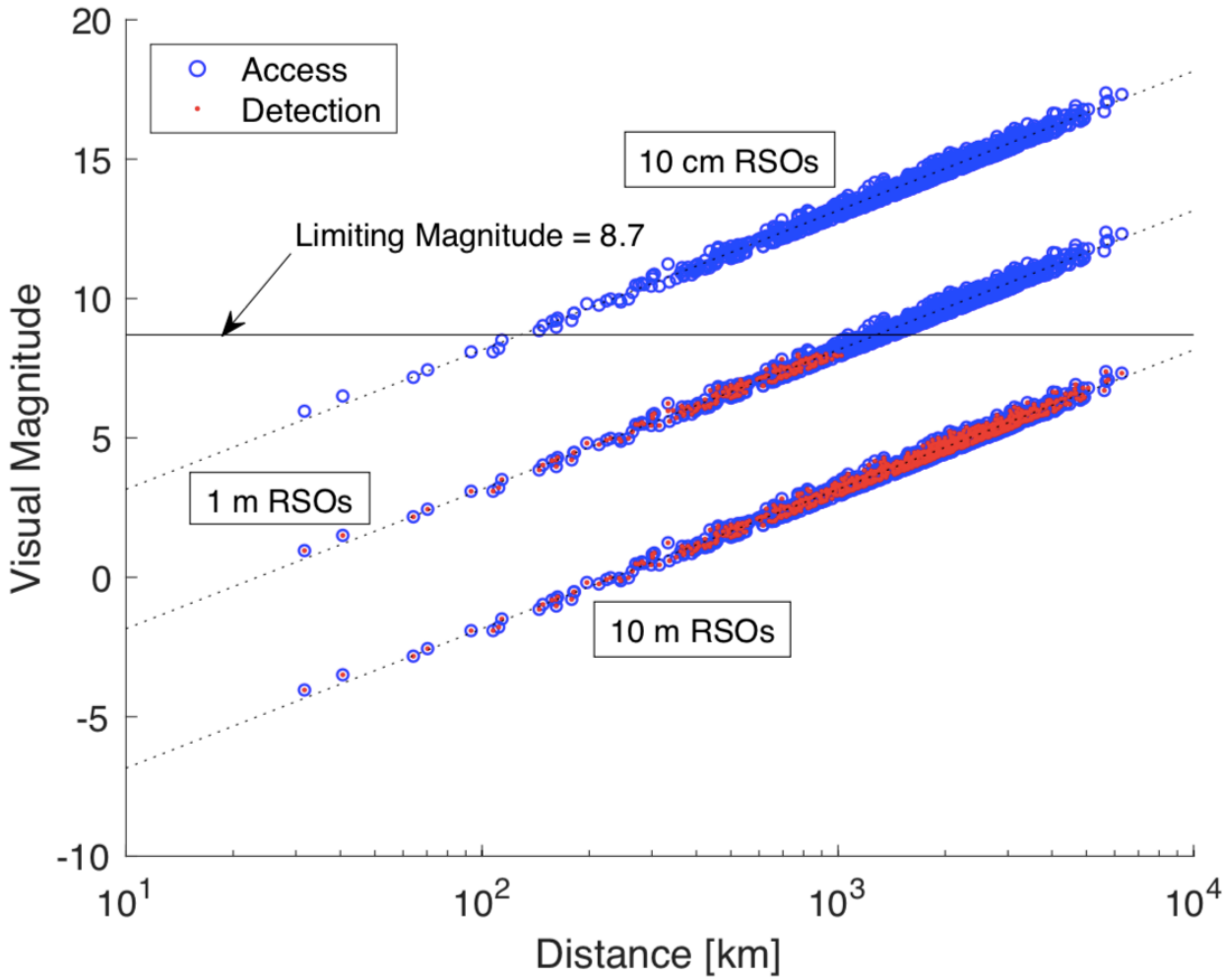

Figure 12: Plot of visual magnitude vs. distance for accesses and detections of the analytic simulator

For the 10 m RSOs, every RSO that was accessed was also detected. The RSO with the dimmest visual magnitude (from the 10 m RSOs) is approximately 7.5 visual magnitudes. The reason that all of the 10 m RSOs were detected is that they were all below the limiting magnitude of the sensor. For the 1 m RSOs, it is clear to see where the sensor stops detecting the RSOs. It stops detecting RSOs at a visual magnitude just below 8.7. Looking at the 10 cm RSOs, it is clear to see that there were no detections. The brightest 10 cm RSO is at a visual magnitude of about 6, which is below the limiting magnitude of the sensor. This object, while being under the limiting magnitude of the sensor was also very close to the sensor (~30 km) and moving at a relative angular

velocity of about 9 deg/sec. This high relative angular velocity reduced the SNR of the RSO to 4.75 (just under the SNR threshold of 6). The angular velocity of the RSO also explains why there is a slight gap between the detections of the 1 m RSOs and the limiting magnitude of 8.7. Some of the RSOs were a magnitude brighter than 8.7 but their relative angular velocities caused their SNRs to decrease and be undetected.

The two tests described above validate the analytic simulator. The first test demonstrated that the simulator was determining when RSOs were in the FOV of the sensor. The start and end of access times were determined with an RMS error of 0.5 seconds. Figure *12* shows that the objects detected by the FAI sensor are all under its limiting magnitude. The dimmest object detected by the sensor had a visual magnitude of approximately 8, slightly brighter than the calculated limiting magnitude of 8.7 which is expected because the movement of the RSOs relative to the sensor lowers the actual SNR of the RSO and prevents it from being detected. Accesses are being determined correctly and of the RSOs that are accessed, only those within the limiting magnitude of the sensor are being detected.

Based on the above verification, the analytic simulator is proven to be suitable for estimating the detection rates of star trackers (and other sensors). Given the parameters of a sensor, a host satellite, the orientation of the sensor, the scenario date and time as well as a list of RSO TLEs, the analytic simulator can determine which RSOs will cross the field of view of the sensor by propagating the orbits of each RSO and the host satellite. Making assumptions about the diameters of the RSOs, the simulator is also able to estimate the detection rate of the sensor by calculating the SNR of each RSO that crosses the field of view of the sensor. The detection rates provided

by the simulator can then be used to draw conclusions about the feasibility of star trackers for RSO detection.

Chapter 4: Image Simulator Description

The main objective of the image simulator is to generate simulated star tracker images. If star trackers are actually to be used for RSO detection, then algorithms will need to be developed to identify whether or not an image contains an RSO in it or not. Images from star trackers will be required to develop the algorithms. Currently, star tracker images are not readily available. When being used for attitude determination, full images are not required to be downloaded to the ground from the spacecraft so images from star trackers on-orbit are not easy to get. The purpose of the image simulator is to provide a source for images for the testing and development of RSO detection algorithms. Similar to the analytic simulator, the algorithm was developed as a MATLAB function and takes almost identical inputs. The only difference between the inputs of the two algorithms is that the image simulator does not take the scenario start and stop times as an input, it simply takes the time that the image exposure is to begin. It also requires the analog-to-digital converter resolution and the gain of the sensor to be provided as inputs. The image simulator is composed of over 1,500 lines of code and consists of 42 sub-functions created for the simulator (some of those functions are the same ones created for the analytic simulator). It also uses the SGP4 functions for orbit propagation and a handful of other functions that come with the SGP4 code [48]. The simulator propagates the host satellite and RSOs to the given date and time (using the SGP4 propagator), determines which RSOs and stars are in the image and then generates the image. It breaks up the exposure time interval in to step sizes based on the fastest moving RSO within the image. The faster the RSOs are moving, the smaller the time step used by the simulator. For each step, the number of photoelectrons

produced on each pixel of the detector from RSOs, stars, background light and noise are calculated. Each of the steps are then combined to get the photoelectrons produced on each pixel for the entire integration time. This approach of breaking the integration time up in to steps allows the simulator to track the motion of the RSOs and stars across multiple pixels. The image simulator can be run independently but if desired it can also be run based on the outputs of the analytic simulator or based on the outputs of previous image simulations.

The image simulator has several outputs. The most significant output is the actual image. The image is returned as an array where each element of the array corresponds to a pixel of the detector and its monochrome intensity. Another important output of the image simulator is an array that contains the ID and pixel location of each RSO that is contained within the image. This array allows the RSOs to be identified and located within the image. As well as these two outputs, the simulator also returns the star tracker, host satellite and mission parameters all contained within a structure and a list of all of the RSOs also contained within a structure (for further image simulation).

4.1 Technical Considerations of the Image Simulator

The simulator takes into consideration the Earth and Moon; reflected solar light from the Earth and Moon; stars and RSOs; the motion of the stars, RSOs and host satellite; background zodiacal light; hot pixels; dark current; non-uniformity in noise sources (dark current, signal and background shot noise, read noise); and a DC background offset. The non-uniformity in noise sources is modeled as a gaussian distribution with a mean of zero and a variance equal to the square root of the sum of the squares of each source (i.e., $variance = \sqrt{\delta_{dark} + \delta_{signalShot} + \delta_{BGShot} + \delta_{read}}$). For

each pixel the noise sources are evaluated, and a random value is generated from the gaussian distribution. Each pixel has a different gaussian distribution associated with it according to the different signal and background sources in its field of view.

Two parameters that are not needed for the Analytic Simulator but are required for the Image Simulator are the analog-to-digital converter (A/D) resolution (bit resolution) and the gain. The A/D resolution is the number of bits that is used by the detector. It is used to set the maximum pixel value (i.e., digital number, DN) for the images. The maximum pixel value (saturation) is:

$$saturation = 2^{bits} - 1 \tag{19}$$

The default value used by the simulator is 16 bits which corresponds to saturation at a pixel value of 65535. This means that a pixel could have a value from 0 to 65535. The gain of the sensor converts a pixel's electron count to digital numbers (pixel values). The simulator determines how many electrons are collected by each pixel (based on the visual magnitude of objects in the field of view of the pixel, noise sources, background light, etc.). The gain is used to convert this electron count into digital numbers. The units of the gain are [e^-/DN]. The default gain used by the simulator is 1.4 [e^-/DN]. These default values are based on the FAI imager which was used for the verification and validation of the image simulator but can be changed by the user.

The image simulator also needs to simulate the point spread function of the sensor. Stars and RSOs, which are small enough to be considered as point sources, do not appear as point sources in images. Due to imperfections in the optical system of the sensor, point sources affect multiple pixels in an image, not just the pixel that they are over. The simulator uses a 3x3 pixel area to generate the point spread function of stars

and RSOs. The point spread function spreads the photons produced by an object over the 3x3 region and is modelled using a two-dimensional gaussian distribution with an amplitude of I_o and a standard deviation of σ. The simulator takes the image coordinates of the object (star or RSO), determines which pixel it is over and finds the centroid (the coordinates of the centre) of each of the pixels in the 3x3 pixel area surrounding the pixel that contains the object. For each pixel in the 3x3 point spread function, the contribution of the object to the pixel is determined by calculating the value of the two-dimensional gaussian based on the distance of the centroid from the object's location as seen in Equation 20.

$$I_p = I_o e^{-\left[\frac{(x_p - x_o)^2 + (y_p - y_o)^2}{2\sigma^2}\right]} \tag{20}$$

In the equation above, I_p is the contribution of the object to the pixel's value, I_o is the amplitude of the gaussian function, x_p and y_p are the centroid coordinates of the pixel, x_o and y_o are the coordinates of the object and σ is the standard deviation of the gaussian function. For each pixel in the point spread function, its calculated I_p value is multiplied by the number of photons produced by the object to get the number of photons that the object contributes to the pixel.

The simulator uses an amplitude of 0.6 and a standard deviation of 0.4 for the point spread function. These values were found by testing a range of amplitudes and standard deviations and comparing them with real images of stars. An amplitude of 0.6 and standard deviation of 0.4 were the values that caused the simulator to recreate the magnitude of the stars as closely as possible. The point spread function described

above is the one that was used for this thesis. However, the simulator could be adapted to support a variety of point spread functions.

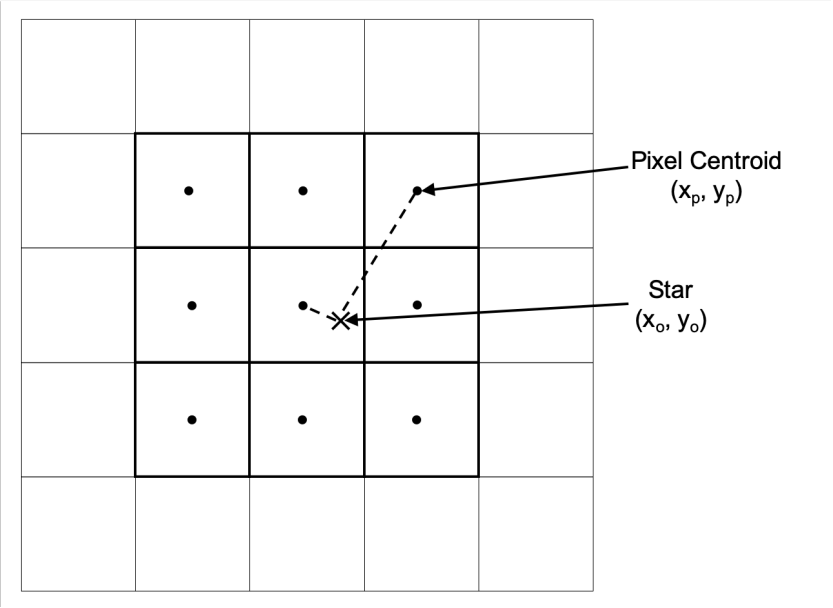

Figure 13: Point Spread Function

The generated image contains a header with information about the image. The header contains the date and time of the start of the exposure; the exposure time in seconds; the number of pixels in the image; the signal range (in DN); the latitude, longitude and altitude of the host satellite; the field of view half angle of the sensor; the coordinate system being used to define the satellite's attitude; the satellite yaw, pitch and roll angles; the three Euler angles used to define the sensor's pointing relative to the satellite; and the right ascension and declination of the boresight. The header is shown below:

SIMULATED IMAGE 2018-03-06 08:46:19 UT
Exp=0.100 256x256 DN=4285-65536
SC lat/lon/alt: 79.9°/-128.5°/1097km FOV Half Angle = 13.8°
Coordinate System: orbital SC YPR: -2.6°/-60°/-39.9°
ST $\theta_x/\theta_y/\theta_z$: -60°/-90°/0° Boresight RA/DEC: 119.6°/-29.6°

Figure 14: Simulated Image Header

The simulator uses Version 5 of the Bright Star Catalogue [69]. The bright star catalogue provided an adequate database of 9,119 stars of magnitude 7 or greater. The data were easily accessible, and the star coordinates were in a convenient coordinate system (J2000 coordinates). The simulator also adds a non-zero electronic direct current (DC) offset to the image. When taking images, an offset can be added to the pixel values (number of electrons) to avoid getting zero values for pixels after going through the analog-to-digital conversion process [70]. The default offset is 4293 [DN]. The default is modeled by the offset produced in level 0 FAI images.

4.2 Sample Simulated Images

Below are figures of sample simulated images. Each figure demonstrates a different component of the image simulator: effect of exposure time on stars, RSOs and noise; Earth and atmospheric glow; the Moon; hot pixels and multi-pixel radiation events (MRE). These figures help to show a few of the major considerations of space-based imaging as well as how the simulator represents them.

Figure *15* shows the effects of varying the exposure time of the image simulator. Stars (a total of 8) and RSOs (a total of 38) in the image on the left are seen as faint points. As the exposure time increases the stars all begin to streak downward and RSOs streak in varying directions. As the exposure time increases the amount of background light collected by the detector also increases.

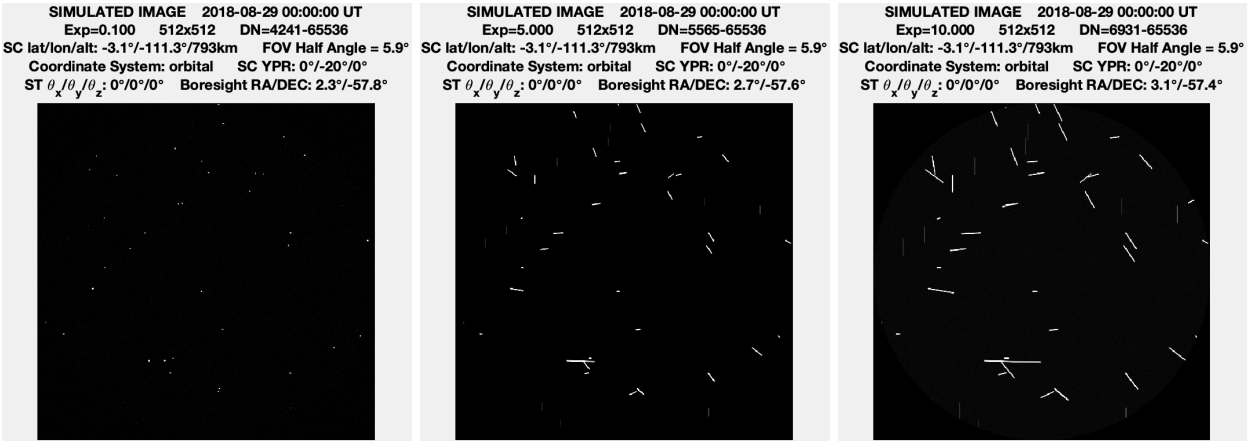

Figure 15: Varying Exposure Time (Left: 0.1 s, Mid: 5 s, Right: 10 s)

Figure 16 shows the Earth glow (light reflected by the Earth and its atmosphere). The dark gray portion of the image in the bottom left is the Earth. Note that an appropriate model for the brightness of the Earth itself has not been developed. For the purposes of the image simulator however the fidelity of the brightness of the Earth itself is not crucial, as RSO detections in front of the limb are not considered to be viable. The white strip above the Earth is Earth glow. It extends only as far as the atmosphere extends off the surface of the Earth (~100 km).

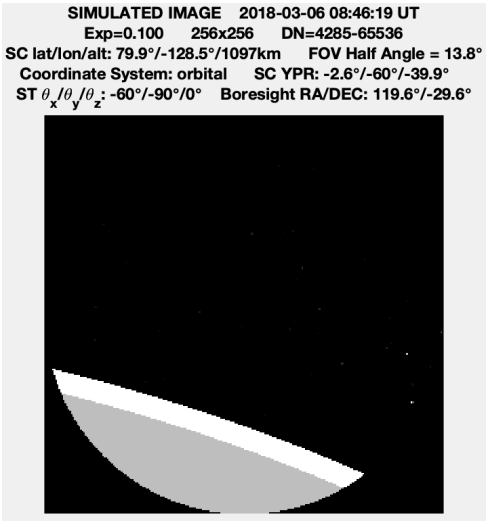

Figure 16: Earth Glow

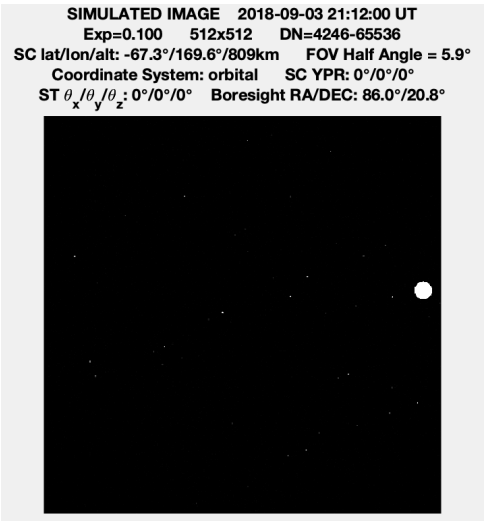

Figure 17: Moon in the Field of View of a star tracker

The Moon is also modelled by the image simulator and can be seen in Figure 17. A surface brightness of 3.05 mv/arcsec^2 is used for the moon. This surface brightness is the brightest surface brightness found for the moon in 2018 using NASA's Jet Propulsion Lab's Horizon web-interface [71]. The brightest value is used to make the simulator more conservative.

Figure 18 shows the effect of increasing exposure time on the noise. In the first image (0.1 second exposure) the noise floor is approximately 4298 DN. In the second image (10 second exposure) the noise floor is approximately 7776 DN. The increase in exposure time increases the intensity of the stars, as expected. It also increases the noise produced by the background zodiacal light and the dark current. The dark current used to simulate these images was 529 [e-/pixel/sec].

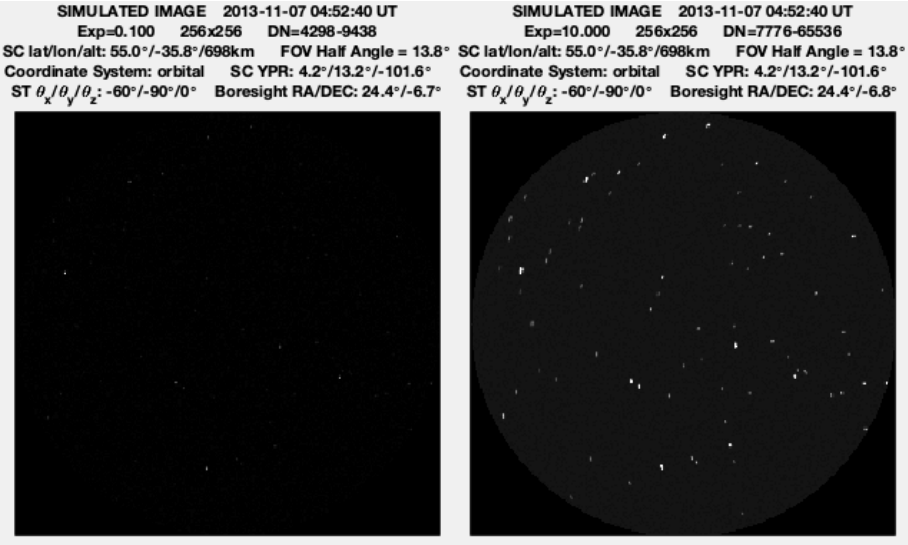

Figure 18: Effect of Increased Exposure Time on Noise

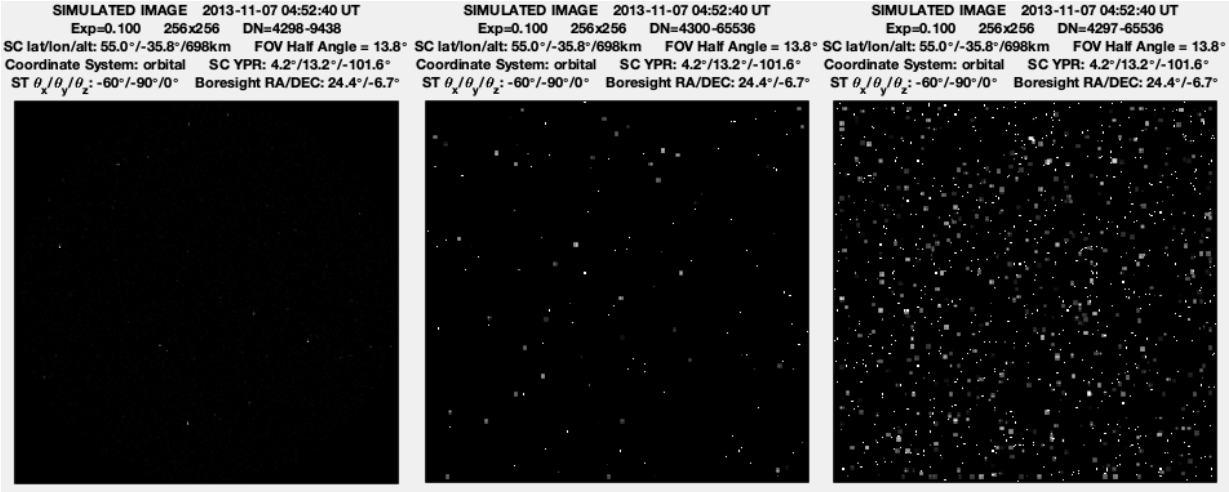

Figure 19: Increased Hot Pixel Density (Left: 0%, Mid: 0.1%, Right: 1%)

Figure 19 shows the effect of the hot pixels and multi-pixel radiation events (MREs) on the simulated images. Each image in Figure 19 has an increased number of hot pixels and MREs. A hot pixel is a single pixel that has a significantly larger dark current than the rest of the image pixels which causes it to have a significantly higher intensity than it should [35]. An MRE is caused by incident radiation on a pixel and results in an increase in intensity for the pixel and its surrounding pixels. The hot pixel and MRE densities are not variables that can be set by user input. It is set within the MATLAB code.

It should be noted that all images shown in this section have different pixel brightness scaling. The scaling has been adjusted to emphasize the relevant features. They are not scaled between the minimum and maximum DN values. A ‘white’ pixel in one image does not necessarily have the same intensity as a ‘white’ pixel in another image. The scaling does not affect the image data itself. Rather than showing the relative brightness of pixels in different images, this scaling ensures that the brightest pixels are visible in the image (even if they would be very faint compared to another image).

4.3 Comparison with FAI

Below is a comparison of RSO positions in real images from the Fast Auroral Imager (FAI) on board Cassiope with images produced by the image simulator. Each image has 256 pixels with pixel (1,1) being the top left of the image. Coordinates are given in the following format: (row number, column number). Figure 20 shows a side-by-side comparison of seven real and simulated FAI images. Beside each set of images is the time stamp from when the image was taken.

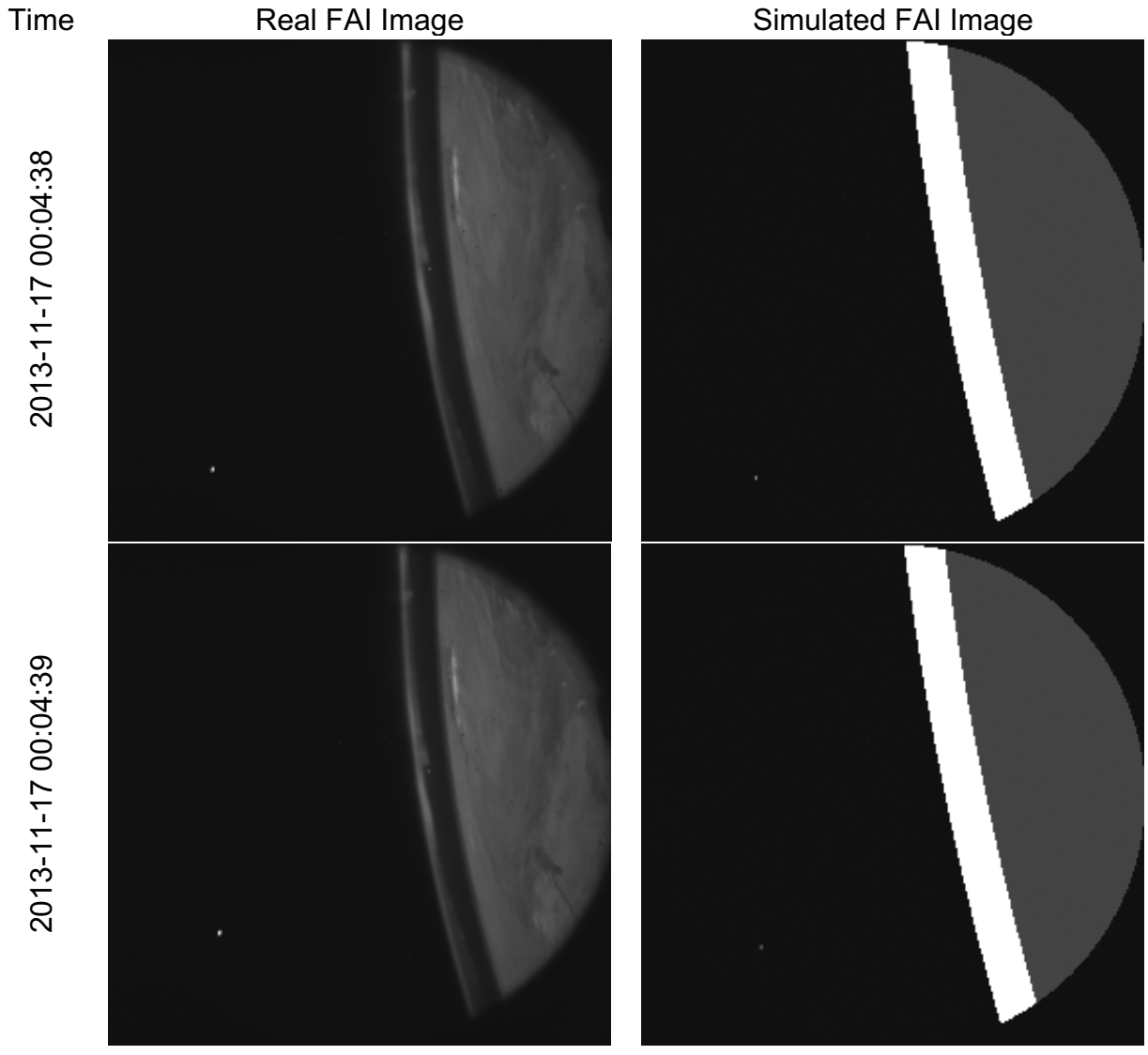

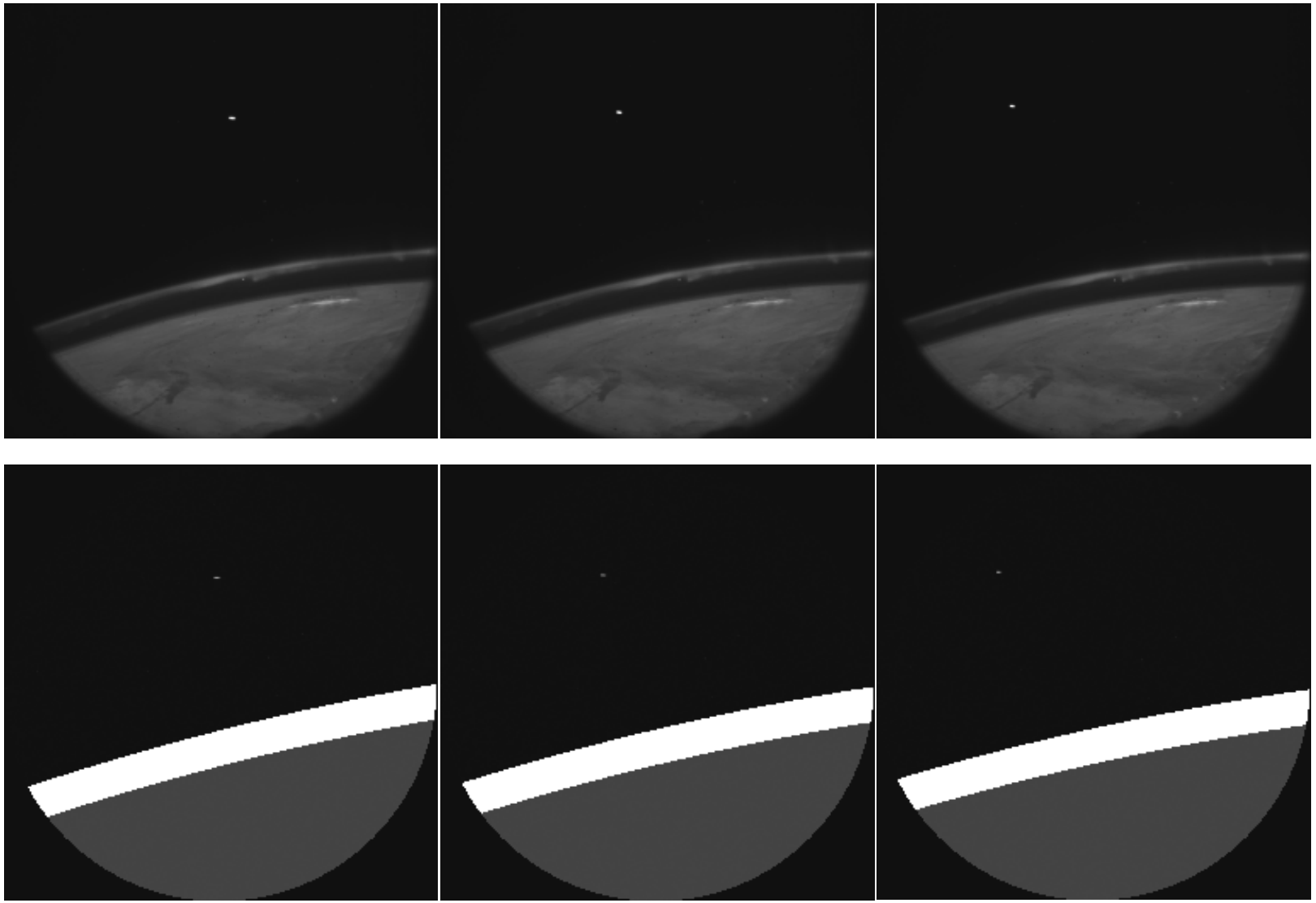
2013-11-17 00:04:42
2013-11-17 00:04:41
2013-11-17 00:04:40

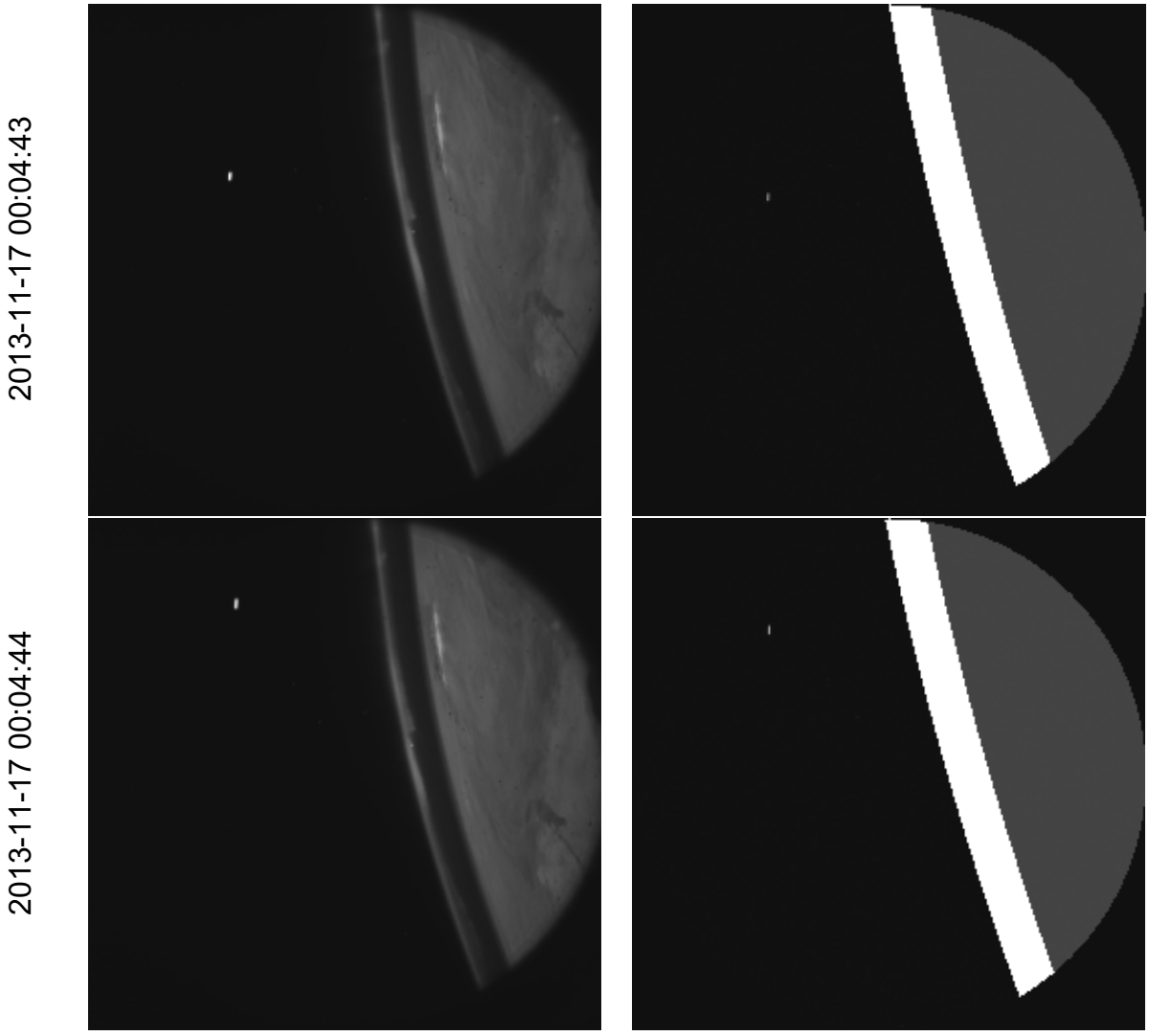

Figure 20: Comparison of Real and Simulated FAI Images

The images above were taken once a second on 2013-11-17 between 00:04:38 UT to 00:04:44 UT. An RSO can be seen as the white point in the bottom left moving from the bottom of the image to the top. The RSO in the image is the METEOR 1-29 satellite shown below. The actual size of METEOR 1-29 is not known but is estimated to be around 5 m by 3 m based on an image of the satellite. The RSO was modelled as a sphere with a diameter of 5 m.

Figure 21: Meteor 1-29 satellite [72]

It is noted that the brightness of the Earth itself should be ignored in the simulated images. A good model for the brightness of the Earth has not been developed. The limb (i.e., the edge) of the Earth is also significantly brighter in the simulated images than the real image. The reason that the simulated limb is significantly brighter than the real images is likely that the simulator treats (for simplicity) every limb as a bright limb and does not distinguish between bright and dark limbs. The images taken by FAI are most likely not taken while pointed at a bright limb but rather at a dark limb.

Table 9: RSO pixel position comparison

Date	Time	FAI		SIM		Delta Row	Delta Col
		Row	Col	Row	Col		
2013-11-17	00:04:38	219	54	224	59	5	5
	00:04:39	199	57	206	62	7	5
	00:04:40	176	61	184	64	8	3
	00:04:41	151	65	160	65	9	0
	00:04:42	122	68	131	67	9	-1
	00:04:43	86	71	98	68	12	-3
	00:04:44	45	74	58	69	13	-5
				RMSE Pixels		**9.4**	**3.7**

The table above compares the pixel positions of the METEOR 1-29 satellite in the real FAI images and the simulated ones. The root-mean-square error (RMSE) of the satellite positions is also shown in the table. The RMSE is used to help the error be understandable in physical quantities (pixels) as opposed to a more abstract value such as a normalized error. The RMSE of the satellite position is 9.4 row pixels and 3.7 column pixels. The error is larger in the row position because the satellite is essentially moving straight up the image and the majority of the error would occur in the direction of motion. The error in RSO positions is relatively small. It is two orders of magnitude smaller than the number of pixels in the rows and columns (256x256). This level of error is small enough to be considered acceptable. From the sample images above and the examination of RSO location, it is clear to see that the simulator is reproducing realistic images accurately.

Magellan Aerospace has been provided with a list of possible future enhancements to the simulator and its capabilities. Based on the above verification, however, the image simulator as developed is proven to produce images that account for the major components of space-based imaging. These components include the relative motion of RSOs and stars with respect to the sensor resulting in streaks in the image, the Earth and its atmosphere, the Moon and hot pixels. Comparison with the FAI sensor on Cassiope also shows that the positions of RSOs in the images are simulated to an acceptable level of accuracy. Given the accuracy of the image simulator and the major components of space-based imaging that it accounts for, it is suitable to be used to generate images for the testing and development of RSO detection and characterization algorithms.

Chapter 5: RSO Detectability Analysis

The analytic simulator was used to determine the feasibility of using a COTS star tracker for detecting the general RSO population. It should be noted that the exact detection rates depend on a lot of different variables such as the sensor parameters, sensor orientation, exposure time, orbit and date. Not all of these variables can be examined in this study. These results are meant to be an estimate of what is achievable for a COTS star tracker so that its feasibility for detecting the general RSO population can be assessed.

Sapphire was used as the host satellite for the simulation. Sapphire is in a Sun-synchronous, polar orbit (common to a lot of satellites, particularly Earth observation ones), has a period of approximately 100 minutes and an altitude between 770 km and 785 km (nearly circular) [6]. The low Earth orbit is thought to be good for on-orbit RSO detection because it provides a good vantage point to image RSOs as it will be closer to the RSOs than a sensor out in GEO, for example. The polar orbit also provides a good view of the North and South poles where many other LEO, polar orbiting RSOs have their orbits converge. The orbit that Sapphire is in is a popular orbit making it a likely destination for a secondary payload star tracker. For these reasons, Sapphire was chosen as the host satellite for these simulations.

The results produced by the simulator are intended to be representative of COTS star trackers in general. To that end, star tracker parameters were selected with the intent of being a fair representation of commercial star trackers that are currently available. The COTS sensor parameters that were used are based on the “modern” star tracker parameters given by Zakharov et al. [32] (modern referring to star trackers being

produced around 2013). Not all parameters that were required for the simulation were provided by Zakharov et al. [32]. The parameters that were not included were substituted using the parameters for the BOKZ-MF star tracker (described in Table 4) because it is classified as a “modern” star tracker by Zakharov et al. [32]. The parameters are given in Table 10.

Table 10: Sample COTS star tracker parameters

Parameter	**Value**
Pixels	512 x 512
Field of View	5.9 deg
QE	0.58*
Optical Transmittance Loss	0.9
Aperture Diameter	1.88 cm
Pixel Size	16 μm
Focal Length	4 cm
Integration Time	0.1 s
Read Noise	22 RMS e-*
Dark Current	400 e-/pixel/second*

* Parameters from the BOKZ-MF star tracker

An RSO catalogue containing all RSOs updated within a day prior to the scenario time (to minimize the effects of propagation errors on the RSOs) and with semi-major axes less than 8,371 km (LEO), was used. Only LEO RSOs were simulated because that portion of the RSO population is easiest to image given its close proximity to the LEO host satellite. The purpose of using COTS star trackers for RSO detection is mainly for detecting LEO RSOs, not MEO, GEO or HEO. Therefore, those portions of the population were excluded. The simulated RSO population had 12,773 RSOs in total. For each simulation that was performed, each individual RSO had its diameter estimated according to method b) described in Section 3.1.3 above.

The simulator study was performed four different times using a different orientation of the star tracker each time in order to examine the effect that different

pointing directions have on the detection rates. Each study was run for a 24-hour period. A 24-hour scenario gives daily rates for accesses and detections which is easily comparable with some of the other RSO detection systems described earlier. The four orientations that were simulated were a ram-facing orientation, an anti-ram-facing orientation, a zenith-facing orientation and an anti-Sun orientation (pointing directly away from the Sun). The ram and anti-ram orientations point along the positive and negative x-axis, respectively, of the orbital coordinate system of the host satellite shown in Figure 7. For Sapphire, in a nearly circular orbit, the x-axis is very close to the ram direction. If a more eccentric orbit was used, then the x- axis would vary from the ram direction. For this scenario however, due to Sapphire's nearly circular orbit, the star tracker can be considered to be pointing in the ram and anti-ram. The ram and anti-ram facing orientations were selected because (with the polar-orbiting Sapphire satellite) they provide a good view of the North and South poles where many orbits of other polar orbiting RSOs intersect. The zenith-facing orientation was selected because it is a more common orientation for star trackers being used for attitude determination. Star trackers are often orientated away from the Earth to avoid light reflected from the Earth interfering with their imaging. This zenith orientation is intended to be representative of a dual-purposed star tracker that is performing RSO detection but is limited by its ADC determined orientation. The orientation pointing directly away from the sun was simulated because it provides the best illumination geometry of RSOs and thus has the potential to provide the best images of RSOs. The results of each simulation are shown in Table 11 below.

Table 11: Simulation results of Four Different Sensor Orientations

		Sim 1	***Sim 2***	***Sim 3***	***Sim 4***
Star Tracker Orientation		Ram	Anti-Ram	Zenith	Anti-Sun
24 Hour Scenario	**Total Accesses**	8,316	4,281	82	5,164
	Unique Accesses	3,952	2,757	82	2,575
	Total Detections	1,237	581	0	800
	Unique Detections	825	425	0	441

Table 11 shows that the performance of the star tracker is largely dependent on its orientation. In terms of total accesses and detections, the ram facing orientation by far outperformed the other orientations. It had approximately twice as many total events (accesses and detections) as the anti-ram and anti-sun orientations. It also accessed and detected almost twice as many unique RSOs. The anti-ram and anti-sun facing orientations performed very similar to each other. The anti-ram facing orientation had more unique events but less total events than the anti-sun orientation which just means that the anti-sun orientation saw fewer individual RSOs but saw those RSOs more often than the anti-ram orientation. The zenith orientation had the poorest performance of all four simulations. It only accessed 82 RSOs and none of those RSOs were detectable by the star tracker.

An unexpected result is that the anti-ram orientation had approximately half of the events that the ram orientation had. The initial assumption might be that it would have approximately the same number of accesses and detections as the ram orientation. As mentioned earlier, a star tracker facing the ram direction likely has most of its RSO observations occur as it approaches the North and South poles where many polar orbits intersect. A star tracker facing anti-ram orientation would presumably see a similar number of objects pass through its field of view as it leaves the North and South poles looking back at where the polar orbits of other RSOs intersect. It is unclear why

the anti-ram orientation has significantly less RSOs passing through its field of view. More work looking at the disparity between the ram and anti-ram orientations would be required to determine its cause. A first approach at finding this cause would include more simulations of the two orientations and recording the location of each access and detection to see where the events take place and if that can provide some explanation for the differences in accesses and detections.

Table 12: Results converted to percentages

	Sim 1	**Sim 2**	**Sim 3**	**Sim 4**
Star Tracker Orientation	Ram	Anti-Ram	Zenith	Anti-Sun
Percent of entire simulated population uniquely accessed	30.9%	21.6%	0.6%	20.2%
Percent of entire simulated population uniquely detected	6.5%	3.3%	0%	3.5%
Percent of all accesses that were detected	14.9%	13.6%	0%	15.5%

To better understand the effectiveness of the COTS star tracker at detecting RSOs, the results in Table 11 were used to determine (1) the percentage of the entire simulated population (12,773 RSOs) that was uniquely accessed, (2) the percentage of the entire simulated population that was uniquely detected and (3) the percentage of accessed RSOs that was also detected. Each of these three parameters (shown in Table 12) are dependent on the orientation and characteristics of the star tracker to differing degrees. The percentage of uniquely accessed RSOs (the first parameter) speaks more to the effectiveness of a given orientation than of the star tracker itself. The only star tracker characteristic that this depends on is the field of view. The percentage of all accessed RSOs that was detected (the third parameter) speaks mainly to the effectiveness of the star tracker itself to detect objects and less on the orientation

of the sensor because it is looking at how well the star tracker detected RSOs that were in its field of view (regardless of how many RSOs didn't fall within the field of view). The only dependence this parameter has on the orientation comes from the distance from the RSO to the star tracker. Some orientations are likely to access objects that are in general closer to the host satellite than another orientation. The ram facing orientation for example may access relatively close objects as Sapphire approaches Earth's North and South poles. The zenith facing orientation on the other hand may access objects that are relatively farther away because it is looking away from Earth. The percentage of the entire simulated population that was uniquely detected (the second parameter) is somewhere in between the other two parameters, dependent on both the orientation and the characteristics/sensitivity of the star tracker itself.

Table 12 also shows that the ram orientation had 30.9% of the simulated RSO population (not including repeated RSOs) passing through its field of view in 24 hours while the anti-ram, anti-Sun and zenith orientations had 21.6%, 20.2% and 0.6%, respectively, of the simulated population pass through their fields of view which reinforces the superiority of the ram facing orientation that was already mentioned. It had over 30% of the LEO population pass through its field of view while the anti-ram and anti-sun orientations only had one fifth of the LEO population pass through their fields of view.

It is important to note that, although the ram facing orientation had nearly twice as many RSOs pass through its field of view as the anti-ram and anti-sun orientations, all three orientations detected between 13% and 16% of all RSOs that passed within their fields of view which is perhaps not a surprise with the ram and anti-ram

orientations as they are observing objects at similar distances. However, the anti-Sun orientation has the ideal viewing geometry from which observations should be made. Despite having better observing geometry, the anti-Sun orientation detected approximately the same percentage of objects passing through its field of view as the ram and anti-ram orientation which could mean one of two things. It could mean that either the viewing geometry is not very significant, or the anti-sun orientation is observing RSOs at distances greater than those from the ram and anti-ram orientations, distances that are great enough to counteract the benefits of the improved viewing geometry.

As stated above, the zenith facing orientation was simulated in an attempt to represent a star tracker being dual-purposed for both ADC and RSO detection. If a star tracker were to be dual-purposed, its orientation would be dictated by the need for ADC and therefore have a zenith facing (or similar orientation). Based on the results given in Table 11 it is clear to see that the zenith facing orientation is not ideal for a star tracker trying to detect RSOs. In 24 hours only 82 of the 12,773 RSOs passed through its field of view. On top of that, the star tracker was not able to detect a single one of the RSOs that passed through its field of view. There are a number of factors that would influence the star tracker's inability to detect the RSOs in this orientation. It is possible that the RSOs were too far away, moving too fast or were simply too small to be detected by the star tracker. Because of the combination of how few RSOs crossed the field of view and how exactly they passed through it (far enough away and fast enough that they were undetectable), the zenith facing orientation does not seem like a promising orientation for RSO detection. Part of the issue, however, with the zenith orientation could have

been the altitude of the orbit it was in. The altitude of the orbit varied from 770 km to 785 km. Many of the RSOs may have been below this altitude and completely undetectable by the star tracker. A zenith orientation combined with an altitude around 400 km might provide better results by allowing more RSOs to pass over (and through) the field of view of the star tracker.

A star tracker being used as a dedicated sensor with the ability to be placed in a favourable orientation could provide very good detection rates as seen with the ram, anti-ram and anti-sun orientations. The poor results for the zenith facing orientation do not look good for the prospect of dual-purposing star trackers to detect RSOs when they are not being used for ADC. The orientation used by star trackers (if in fact, a zenith orientation is a fair representation of it) does not appear to be good for detecting RSOs. However, this should be examined further by simulating a lower altitude host satellite before drawing any conclusions about a dual-purposed star tracker in a zenith facing orientation.

Chapter 6: Conclusions

The issue of a growing RSO population that is crowding the environment around Earth shows no signs of slowing down. More and more satellites are launched into space and the threat of collision is continually increasing. A collision threatens massive financial loss, loss of the capabilities of the satellite (communications, GNSS, remote sensing, etc.) and an even more dangerous environment as fragmentation debris would be scattered from the collision. Attempts at cataloguing, tracking and predicting the current RSO population have been successful but there are still gaps in the coverage provided by these attempts. With the current network of ground and space-based sensors, not all areas of space around Earth are observable at every instant in time. A potential way to complement the networks and sensors already being used is to employ the use of star trackers as RSO detection sensors. This thesis has examined the feasibility of star trackers to be used for RSO detection. The main points that have been discussed are:

- The advantage of star trackers is found in their low cost compared to dedicated RSO detection systems
- The analytic simulator has been developed for detection rate estimation (to determine feasibility)
- The image simulator has been developed for RSO detection and characterization algorithm development
- A wide range of detection rates by star tracker's is possible. These rates depend on mission parameters with the orientation of the star tracker being very significant

- The goal of 1-10 detections per day that defines the feasibility of a star tracker for detecting the general RSO population is achievable and can be greatly exceeded
- The feasibility of dual purposing a star tracker is inconclusive (due to the inconclusive results of the zenith orientation)
- A dedicated star tracker (i.e., a star tracker which can be put in a favourable orientation) is feasible for RSO detection of the general population

Based on the results presented in this thesis, it is possible to draw conclusions about the feasibility of using COTS star trackers for RSO detection and tracking. It is clear from the results that a wide range of detection rates is possible depending on the scenario parameters. A significant factor in those detection rates is the orientation of the star tracker (which may or may not be able to be controlled depending on the satellite and mission that the star tracker is on). In the four simulated scenarios, there were detection rates ranging from zero detections per day to over 1,200 detections per day, with over half of those detections (825) being unique detections. The mission parameters (particularly the sensor orientation) are important variables and need to be carefully selected.

Comparing the results from the simulations with the goal of 1-10 RSO detections per star tracker per day it is clear to see that this goal is attainable. However, detection rates depend on many different factors and this detection rate is not always attainable as can be seen with the zenith facing orientation. In a 24-hour scenario it did not detect any RSOs. The other simulations, on the other hand, greatly exceeded the goal indicating that unique detection rates of approximately 400 RSOs per day to over 800 RSOs per day are possible. This detection rate means that it is possible for a single star

tracker to update almost one thousand unique RSOs (approximately 5% of the entire RSO population). It would continue to update the majority of that 5% on a recurring basis because of the periodicity of the RSO and host satellite orbits. Detection rates can increase to over 1,200 RSOs per day when looking at total detections.

A dual-purposed star tracker for ADC and RSO detection may not be feasible because very few RSOs actually pass through its field of view and those that do are undetectable (assuming that the zenith facing orientation is an accurate representation of a star tracker being used for ADC). However, further study of the effect that the altitude of the star tracker has on the zenith facing orientation should be done before definitively saying that dual-purposed star trackers are not feasible. On the other hand, one dedicated star tracker can detect as many as 1,200 RSOs per day. This impact is compounded by the possibility of a constellation of dedicated star trackers. Each star tracker could potentially have unique objects that only it is able to detect. However, they could also potentially detect the same objects at different times, providing more updates than a single sensor would. Dedicated star trackers could be placed in specific orbits to detect RSOs that are not easily detectable from the ground. The potential that star trackers have at detecting RSOs goes beyond the range of this research but is worth pursuing.

The benefit of using star trackers for RSO detection is that they are significantly cheaper than dedicated sensors and easier to obtain. With a detection rate of 1,200 RSOs per day, the cost per observation for a star tracker with an annual cost of US$100,000 (the expensive case considered in Section 2.7) is $0.23, significantly less expensive than the dedicated ground and space-based sensors that were compared.

The cheapest dedicated system was the GEODSS network at $0.76 per observation. If star trackers can be used to fill in some of the spatial and temporal gaps left by dedicated ground and space-based sensors, they may be able to do it at a fraction of the cost. Their ability to be bought off the shelf allows them to be obtained quickly, without the cost and time associated with developing dedicated sensors. Star trackers are not intended to replace any existing dedicated sensors. A dedicated sensor designed for space-based RSO detection could significantly outperform a star tracker because star trackers are not designed for this purpose. Star trackers are significantly less sensitive than these dedicated systems because a high level of sensitivity is not required for attitude determination. A star tracker would not be able to detect more RSOs than a dedicated sensor and it is not likely that it would detect any new objects that have not already been tracked and catalogued at some point in the past (though it is possible). The advantage of star trackers is their cost and accessibility. The low cost and ease of accessibility of star trackers allows them to be put in place quickly and at a low cost, producing constellations of star trackers, that will hopefully be able to fill in gaps in RSO coverage and reduce the time between detections. Reducing the time between detections provides more recent TLEs, increases the accuracy of position estimates and reduces the number of conjunction reports (collision warnings) that satellite operators get.

Given the feasibility suggested by this research, further work should be pursued. This thesis establishes the feasibility of star trackers to be used to detect the general RSO population. For star trackers to be most effective they should be able to detect the

un-updated portion of the RSO population. To establish the feasibility of star trackers to detect the un-updated portion of the RSO population several steps are still required:

- Identify the RSOs that are not updated on a regular basis
- Determine the ideal orbital and mission parameters for a star tracker to best fill in those gaps
- Assess the star tracker's ability to fill in the identified gaps given the ideal parameters

Determining which RSOs need to be updated more regularly and which areas of the sky need better coverage should be determined first. After these gaps have been determined then the orbits and orientations that are best suited to filling in those gaps can be found. Using the analytic simulator, ideal mission parameters (host satellite orbit, star tracker orientation, etc.) should be determined for star trackers to fill in these gaps. Finally, the star tracker's ability to fill in the identified gaps using the ideal parameters needs to be assessed so that it can be determined how cost-effective the star tracker really is. These three tasks need to be completed before conclusions on the feasibility of star trackers for filling in gaps left by the current networks can be drawn.

There are more questions that should be considered to help assess the effectiveness of star trackers for RSO detection. The benefits of constellations of star trackers should be investigated to determine how to maximize the efficiency of RSO detections. It would also be useful to investigate the long-term effects of a star tracker. How variable is the detection rate of a star tracker over time? Do new RSOs become detectable over time as orbits drift or as RSOs move into "sync" with the

star tracker (due to orbits with slightly different periods)? Do some RSOs move out of “sync” with the star tracker and become undetectable?

Work has already begun in the areas of RSO detection, tracking, identification and characterization from COTS star trackers. The image simulator is being used to test detection algorithms as well as algorithms that determine the shape, attitude and spin rate of RSOs to characterize them. It is hoped that as these areas progress and further research in the feasibility of star trackers is done, star trackers will soon begin to be used to complement the detection efforts already being done by ground and space-based networks. In doing so, mission planners and operators can continue to launch spacecraft with up to date knowledge of the environment that they are launching in to, creating a more sustainable space environment for the future.

References

[1] N. V. Patel, “NASA isn’t happy about India’s anti-satellite missile test,” *Popular Science*, 05-Apr-2019. [Online]. Available: https://www.popsci.com/india-anti-satellite-missile-test-space-debris. [Accessed: 08-May-2019].

[2] “Orbital Debris Program Office - Frequently Asked Questions,” *NASA Astromaterials Research and Exploration Science*, 12-Apr-2019. [Online]. Available: https://orbitaldebris.jsc.nasa.gov/faq/. [Accessed: 26-Sep-2017].

[3] P. Anz-Meador, “Orbital Debris Quarterly News,” *NASA Orbital Debris Program Off.*, vol. 22, no. 1, Feb. 2018.

[4] “Handbook for Limiting Orbital Debris.” National Aeronautics and Space Administration, 30-Jul-2008.

[5] “About Space Debris,” *European Space Agency*. [Online]. Available: https://www.esa.int/Our_Activities/Operations/Space_Debris/About_space_debris. [Accessed: 03-Apr-2018].

[6] “Space-Track,” *Space-Track*. [Online]. Available: https://www.space-track.org/. [Accessed: 26-Sep-2017].

[7] “Environment,” *CNES Space Debris*. [Online]. Available: https://debris-spatiaux.cnes.fr/fr/node/116. [Accessed: 20-Jul-2019].

[8] *Technical Report on Space Debris*. New York: United Nations, 1999.

[9] “Scanning and Observing,” *European Space Agency*, 14-Apr-2017. [Online]. Available: http://www.esa.int/Our_Activities/Operations/Space_Debris/Scanning_and_observing2. [Accessed: 15-Sep-2017].

[10] “USSTRATCOM Space Control and Space Surveillance,” *U.S. Strategic Command*, 17-Oct-2016. [Online]. Available: http://www.stratcom.mil/Media/Factsheets/Factsheet-View/Article/976414/usstratcom-space-control-and-space-surveillance/. [Accessed: 07-Nov-2017].

[11] D. McKissock and C. Wilson, “18th Space Control Squadron Mission Brief,” Apr-2017.

[12] M. R. Ackermann, C. R. R. Kiziah, P. C. Zimmer, J. T. McGraw, and D. D. Cox, “A Systematic Examination of Ground-Based and Space-Based Approaches to Optical Detection and Tracking of Satellites,” presented at the Space Symposium, Colorado Springs, Colorado, United States of America, 2015, p. 46.

[13] “NEOSSat: Canada’s Sentinel in the Sky,” *Canadian Space Agency*. [Online]. Available: http://www.asc-csa.gc.ca/eng/satellites/neossat/default.asp. [Accessed: 28-Sep-2017].

[14] “NEOSSat,” *Earth Observation Portal*. [Online]. Available: https://directory.eoportal.org/web/eoportal/satellite-missions/n/neossat. [Accessed: 07-Nov-2017].

[15] “NEOSSat’s Dual Mission – HEOSS,” *NEOSSat*. [Online]. Available: http://neossat.ca/?page_id=99. [Accessed: 15-Sep-2017].

[16] “Sapphire,” *Earth Observation Portal*. [Online]. Available: https://directory.eoportal.org/web/eoportal/satellite-missions/s/sapphire-space-surveillance#sensors. [Accessed: 16-Oct-2017].

[17] “Space Based Space Surveillance,” *Air Force Space Command*, 22-Mar-2017. [Online]. Available: http://www.afspc.af.mil/About-Us/Fact-Sheets/Display/Article/249017/space-based-space-surveillance/. [Accessed: 03-Apr-2018].
[18] “SBSS (Space-Based Surveillance System) - Satellite Missions - eoPortal Directory,” *Earth Observation Portal*. [Online]. Available: https://eoportal.org/web/eoportal/satellite-missions/content/-/article/sbss. [Accessed: 16-Oct-2017].
[19] D. C. Harrison and J. C. Chow, “The Space-Based Visible Sensor,” *Johns Hopkins APL Tech. Dig.*, vol. 17, no. 2, p. 227, 1996.
[20] “Geosynchronous Space Situational Awareness Program,” *Air Force Space Command*, 22-Mar-2017. [Online]. Available: http://www.afspc.af.mil/About-Us/Fact-Sheets/Display/Article/730802/geosynchronous-space-situational-awareness-program/. [Accessed: 03-Apr-2018].
[21] “Space Tracking and Surveillance System (STSS),” *Missile Defense Advocacy Alliance*, Dec-2018. [Online]. Available: http://missiledefenseadvocacy.org/missile-defense-systems-2/missile-defense-systems/u-s-deployed-sensor-systems/space-tracking-and-surveillance-system/. [Accessed: 23-Jan-2019].
[22] “Space-Based Infrared System (SBIRS),” *Missile Defense Advocacy Alliance*, Dec-2018. [Online]. Available: http://missiledefenseadvocacy.org/missile-defense-systems-2/missile-defense-systems/u-s-deployed-sensor-systems/sbirs-geo-1/. [Accessed: 24-Jan-2019].
[23] J. R. Shell, “Optimizing Orbital Debris Monitoring with Optical Telescopes,” US Air Force, Space Innovation and Development Center, Sep. 2010.
[24] H. Karttunen, P. Kröger, H. Oja, M. Poutanen, and K. J. Donner, Eds., *Fundamental Astronomy*, Fifth Edition. New York: Springer, 2016.
[25] W. E. Krag, “Visible Magnitude of Typical Satellites in Synchronous Orbits,” Massachusetts Institute of Technology Lincoln Laboratory, Lexington, Massachusetts, Sep. 1974.
[26] M. D. Hejduk, “Specular and Diffuse Components in Spherical Satellite Photometric Modeling,” in *Proceedings of the Advanced Maui Optical and Space Surveillance Technologies Conference*, Maui, Hawaii, 2011.
[27] A. Lohman, “Star Imaging for Nanosatellite Applications,” York University, Toronto, Ontario, 2017.
[28] “Dark Current,” *Teledyne Photometrics*. [Online]. Available: https://www.photometrics.com/resources/learningzone/darkcurrent.php. [Accessed: 03-May-2018].
[29] “Signal-to-Noise Ratio,” *Teledyne Photometrics*. [Online]. Available: https://www.photometrics.com/resources/learningzone/signaltonoiseratio.php. [Accessed: 03-May-2018].
[30] R. Downes and S. Rose, “Hubble Space Telescope Primer for Cycle 11.” Space Telescope Science Institute, Jun-2001.
[31] A. Maybhate *et al.*, “ACS Instrument Handbook.” Space Telescope Science Institute, Dec-2010.

[32] A. I. Zakharov, M. E. Prokhorov, M. S. Tuchin, and A. O. Zhukov, “Minimum Star Tracker Specifications Required to Achieve a Given Attitude Accuracy,” *Astrophys. Bull.*, vol. 68, no. 4, pp. 481–493, Oct. 2013.
[33] M. Richmond, “Signal Versus Noise (with illustrations).” [Online]. Available: spiff.rit.edu/classes/phys373/lectures/signal/signal_illus.html. [Accessed: 03-May-2018].
[34] M. D. Hejduk, J. V. Lambert, C. M. Williams, and R. L. Lambour, “Satellite Detectability Modeling for Optical Sensors,” in *Proceedings of the Advanced Maui Optical and Space Surveillance Technologies Conference*, Maui, Hawaii, 2004.
[35] P. Irvin, “CMOS Imager for Nanosatellite Applications,” York University, Toronto, Ontario, 2014.
[36] “Second Generation Star Tracker (ST-16RT2).” Sinclair Interplanetary, 2017.
[37] “Hydra,” *Sodern*, Jun-2017. [Online]. Available: http://www.sodern.com/website/docs_wsw/RUB_255/tile_502/Datasheet_HYDRA_2017.pdf. [Accessed: 03-Oct-2017].
[38] “Hydra-TC,” *Sodern*, Jun-2017. [Online]. Available: http://www.sodern.com/website/docs_wsw/RUB_215/tile_508/Datasheet_HYDRA_TC_2017.pdf. [Accessed: 03-Oct-2017].
[39] “Auriga,” *Sodern*, Jun-2017. [Online]. Available: http://www.sodern.com/website/docs_wsw/RUB_255/tile_502/Datasheet_AURIGA_2017.pdf. [Accessed: 03-Oct-2017].
[40] “Star Trackers,” *Blue Canyon Technologies*. [Online]. Available: http://bluecanyontech.com/wp-content/uploads/2017/07/DataSheet_StarTrackers_05_F.pdf. [Accessed: 02-Oct-2017].
[41] “Autonomous Star Sensor Astro APS.” Jena Optronik, Jan-2015.
[42] “MAI-SS Space Sextant,” *CubeSatShop*. [Online]. Available: https://www.cubesatshop.com/product/mai-ss-space-sextant/. [Accessed: 03-Apr-2019].
[43] “KU Leuven Star Tracker,” *CubeSatShop*. [Online]. Available: https://www.cubesatshop.com/product/kul-star-tracker/. [Accessed: 28-Mar-2019].
[44] “NST-3 Nano Star Tracker,” *CubeSatShop*. [Online]. Available: https://www.cubesatshop.com/product/nst-3-nano-star-tracker/. [Accessed: 28-Mar-2019].
[45] F. Curti, D. Spiller, V. Schiattarella, and R. Orsi, “Recognition of Orbiting-Objects Through Optical Measurements of Light-Reflecting Targets By Using Star-Sensors,” in *IAA Conference on Space Situational Awareness (ICSSA)*, Orlando, FL, USA, p. 20.
[46] K. Bernander, “A Method for Detecting Resident Space Objects and Orbit Determination Based on Star Trackers and Image Analysis,” Uppsala Universitet, Sweeden, 2014.
[47] D. A. Vallado, P. Crawford, R. Hujsak, and T. S. Kelso, “Revisiting spacetrack report# 3,” *AIAA*, vol. 6753, p. 2006, 2006.
[48] T. S. Kelso, “CelesTrak: Astrodynamics Software by David Vallado,” *Celestrak*. [Online]. Available: https://www.celestrak.com/software/vallado-sw.php. [Accessed: 20-Jul-2019].

[49] “CCD47-20 Back Illuminated NIMO Frame-Transfer High Performance CCD Sensor.” Teledyne e2v, 2017.
[50] “CCD47-20 Back Illuminated High Performance AIMO Back Illuminated CCD Sensor.” e2v Technologies, 06-Mar-2006.
[51] “CASSIOPE,” *Earth Observation Portal*. [Online]. Available: https://earth.esa.int/web/eoportal/satellite-missions/c-missions/cassiope. [Accessed: 29-Jun-2018].
[52] “FAI,” *European Space Agency*. [Online]. Available: https://epop.phys.ucalgary.ca/fai/. [Accessed: 08-Apr-2019].
[53] “CCD67 Back Illuminated NIMO High Performance Compact Pack CCD Sensor.” e2v Technologies, 04-Apr-2003.
[54] L. Cogger *et al.*, “Fast Auroral Imager (FAI) for the e-POP Mission,” *Space Sci. Rev.*, vol. 189, no. 1–4, pp. 15–25, Oct. 2014.
[55] M. Prokhorov, M. Abubekerov, A. Biryukov, O. Stekolshchikov, M. Tuchin, and A. Zakharov, “Star Tracker on Chip.” Sternberg Astronomical Institute of Lomonosov Moscow State University and Azmerit Ltd., 2013.
[56] “MT9P031.” ON Semiconductor, Jan-2017.
[57] “MT9P031 Image Sensor.” Micron Technology Inc., 2006.
[58] “Comparative characteristics of the BOKZ family star trackers,” *Space Research Institute of the Russian Academy of Sciences*. [Online]. Available: http://ofo.ikiweb.ru/en/bokz_table.php. [Accessed: 04-Oct-2017].
[59] “The device stellar orientation BOKZ-MF,” *Space Research Institute of the Russian Academy of Sciences*. [Online]. Available: http://ofo.ikiweb.ru/razrabotki/bokz-mf.html. [Accessed: 09-Apr-2019].
[60] “KAF-0261E,” *IEEE Datasheets 360*. [Online]. Available: https://www.datasheets360.com/part/detail/kaf-0261e/2724867437760317009/. [Accessed: 09-Apr-2019].
[61] “KAF-0261.” ON Semiconductor, Mar-2016.
[62] “MSX,” *Earth Observation Portal*. [Online]. Available: https://directory.eoportal.org/web/eoportal/satellite-missions/m/msx. [Accessed: 05-Apr-2019].
[63] R. Leitch and I. Hemphil, “Sapphire: A Small Satellite System for the Surveillance of Space,” presented at the AIAA/USU Conference on Small Satellites, Logan, UT, USA, 2010.
[64] D. A. Vallado and P. J. Cefola, “Two-line element sets - Practice and use,” presented at the International Astronautical Congress, Naples, Italy, 2012, p. 15.
[65] J. R. Wertz and W. J. Larson, Eds., *Space Mission Analysis and Design*, 3rd ed. Microcosm Press ; Springer, 1999.
[66] F. R. Hoots and R. L. Roehrich, “Spacetrack Report No. 3 Models for Propagation of NORAD Element Sets.” 31-Dec-1980.
[67] “SGP4 Propagator,” *STK*. [Online]. Available: http://help.agi.com/stk/index.htm#stk/vehSat_orbitProp_msgp4.htm. [Accessed: 04-Apr-2019].
[68] “e-POP on CASSIOPE,” *European Space Agency*. [Online]. Available: https://epop.phys.ucalgary.ca/. [Accessed: 08-Apr-2019].

[69] “Yale Bright Star Catalog,” *Harvard*. [Online]. Available: http://tdc-www.harvard.edu/catalogs/bsc5.html. [Accessed: 29-Aug-2018].
[70] “Gain, Offset, and Bit Depth,” *Stark Labs*, 04-Jan-2008. [Online]. Available: http://www.stark-labs.com/help/blog/files/GainAndOffset.php. [Accessed: 05-Apr-2019].
[71] “HORIZONS Web-Interface,” *Jet Propulsion Lab California Institue for Technology*. [Online]. Available: https://ssd.jpl.nasa.gov/horizons.cgi#top. [Accessed: 14-Feb-2019].
[72] G. D. Krebs, “Meteor-Priroda,” *Gunter’s Space Page*, 12-Nov-2017. [Online]. Available: https://space.skyrocket.de/doc_sdat/meteor-priroda.htm. [Accessed: 06-Feb-2019].
[73] D. Michaels, “Ball Aerospace Star Tracker Achieves High Tracking Accuracy for a Moving Star Field,” in *Aerospace Conference, 2005 IEEE*, 2005, pp. 1–7.
[74] E. Aretskin-Hariton and A. J. Swank, “Star Tracker Performance Estimate with IMU,” in *AIAA Guidance, Navigation, and Control Conference*, 2015, p. 0334.
[75] “CT-601 High Accuracy Star Tracker.” Ball Aerospace & Technologies Corp.
[76] “Autonomous Star Sensor ASTRO 10.” Jena Optronik, Jul-2015.
[77] “Star Trackers,” *Sinclair Interplanetary*. [Online]. Available: http://www.sinclairinterplanetary.com/startrackers. [Accessed: 04-Oct-2017].
[78] J. Engright, D. Sinclair, C. Grant, G. McVittie, and T. Dzamba, “Towards Star Tracker Only Attitude Estimation,” presented at the Conference on Small Satellites, Logan, UT, USA, 2010.
[79] “Berlin Space Technologies | Star Tracker ST400 and ST200.” [Online]. Available: https://www.berlin-space-tech.com/portfolio/star-tracker-st400-and-st200/. [Accessed: 04-Oct-2017].
[80] “MAI-SS Space Sextant.” Adcole Maryland Aerospace, 2017.
[81] “KU Leuven Star Tracker.” KU Leuven.
[82] “PST-3 Star Tracker,” *TY-Space*. [Online]. Available: http://www.ty-space.com/en/pd.jsp?id=18#_jcp=2. [Accessed: 20-Jul-2019].
[83] “NST-4 Star Tracker,” *TY-Space*. [Online]. Available: http://www.ty-space.com/en/pd.jsp?id=17#_jcp=2. [Accessed: 20-Jul-2019].
[84] D. Piot *et al.*, “HYDRA STAR TRACKER ON-BOARD SPOT-6.” Sodern, 2013.
[85] “Datasheet HYDRA M Sodern,” *Sodern*. [Online]. Available: http://www.sodern.com/website/docs_wsw/RUB_215/tile_508/Datasheet_HYDRA_M_2017.pdf. [Accessed: 03-Oct-2017].
[86] “Star Trackers,” *Sodern*. [Online]. Available: http://www.sodern.com/website/en/ref/Optronic_215.html. [Accessed: 03-Oct-2017].

Appendix A: Parameters for Analytic Simulator Results

Below, in Table 13 and Table 14 are all of the parameters used to run the analytic simulator and get the results shown in Chapter 5. The RSO TLE text file contained 12,773 unique RSOs with epochs from December 31, 2018 or January 1, 2019. All of the RSOs had a semi-major axis less than 8,371 km. The simulations were run for a 24-hour scenario. They were run from January 1, 2019 00:00:00 UTC to January 2, 2019 00:00:00 UTC. A 24-hour scenario was selected so that the detection rates could be interpreted as daily detection rates.

Table 13 shows the parameters that varied between each of the simulations that were done. For each simulation, everything was held constant except for the orientation of the star tracker. The parameters that affect the orientation of the star tracker are “coordSystem”, the coordinate system being used to define the orientation of the star tracker; “yaw”, “pitch” and “roll”, the Euler angles defining the attitude of the host spacecraft in “coordSystem”; and “thetaX”, “thetaY” and “thetaZ”, the Euler angles defining the attitude of the sensor with respect to the host spacecraft’s attitude.

Table 14 shows the parameters that remained constant between each of the simulations. These parameters define the characteristics of the sensor, the RSO diameter estimation method and the RSO reflectivity.

Table 13: Variable parameters used for each simulation from Chapter 5

Parameter	Description	Sim 1	Sim 2	Sim 3	Sim 4
Star tracker boresight orientation	Direction that the boresight of the sensor is pointed	Ram	Anti-Ram	Zenith	Anti-Sun
coordSystem	The reference coordinate system used to define the SC orientation	Orbital	Orbital	Orbital	Anti-Sun
yaw	The Euler angle to rotate the spacecraft about the z-axis of the reference coordinate system (using the right-hand rule)	0	0	0	0
pitch	The Euler angle to rotate the spacecraft about the y-axis of the reference coordinate system (using the right-hand rule)	0	180	90	0
roll	The Euler angle to rotate the spacecraft about the x-axis of the reference coordinate system (using the right-hand rule)	0	0	0	0
thetaX	The Euler angle to rotate about the x-axis of the SC to get the ST orientation	0	0	0	0
thetaY	The Euler angle to rotate about the y-axis of the SC to get the ST orientation	0	0	0	0
thetaZ	The Euler angle to rotate about the z-axis of the SC to get the ST orientation	0	0	0	0

Table 14: Common parameters used for each simulation in Chapter 5

Parameter	Description	Value
pixels	Number of pixels on the detector	512
QE	Quantum efficiency of the detector	0.58
tau	Optical transmittance loss of the detector	0.9
appDiam	Aperture diameter of the detector	0.0188 m
x	Individual pixel dimensions of the detector	0.000016 m
f	Focal length of the detector	0.04 m
t_int	Integration time of the detector	0.1 s
e_n	Read noise of the detector	22 rms e^-
DC	Dark current of the detector	400 e^- /sec/pixel
opLength	The length of time that ST operates during one of its operation/non-operation cycles	60 s
opPercent	The percentage of time that the ST is operating in RSO detection mode during the scenario	100%
diametermethod	The method being used to generate the RSO diameters	4
mean	The mean of the normal distribution being used to generate the RSO diameters (diameter method 1 only)	10 cm
sigma2	The variance of the normal distribution being used to generate the RSO diameters (diameter method 1 only)	50 cm
reflectivity	The reflectivity used to model the RSOs	0.175
lambda0	The beginning of the spectral range of the detector being used	400 nm
lambda1	The end of the spectral range of the detector being used	1000 nm
bits	The number of bits used by the detector	12
eDN	The number of electrons per DN	1.4 e-/DN
Re	The radius of the Earth	6371 km
EEA	The Earth exclusion angle. The angle that the boresight must be away from the limb of the Earth to not have the field of view washed out by Earth glow	10 deg
SEA	The Sun exclusion angle. The angle that the field of view must be away from the limb of the Sun to not have any direct solar light enter	50 deg
DCoffset	The DC offset applied by the image simulator to the image	4293 DN

Appendix B: Survey of Star Trackers

Table 15 shows a survey of star trackers, specifically their limiting magnitude and field of view. The survey is not necessarily exhaustive but includes as many star trackers as could be found. For the star trackers manufactured by Sodern, information on the limiting magnitude and field of view could not be found. The star trackers are still listed to provide as complete a list of star trackers as possible.

Table 15: Survey of star tracker limiting magnitude and field of view

Manufacturer	Model	Limiting Magnitude	Exposure Time (s)	FOV (deg)
Blue Canyon Technologies	Thin Slice NST [40]	7.5	--	10x12
	Standard NST [40]	7.5	--	10x12
	Extended NST [40]	7.5	--	10x12
	MST [40]	7.5	--	10x12
Ball Aerospace	HAST [73], [74]	5.5	0.02	9.47
	CT-601/602 [74], [75]	6	0.1	7.8
Jena Optronik	ASTRO 15 [74]	6.5	0.25	13.25
	ASTRO APS [41]	6	--	20
	ASTRO 10 [76]	6	0.25	16.7x12.5
Moscow Experimental Design Bureau 'Mars'	AD-1 [32]	5-6	0.5	18
Research and Production Enterprize 'Geofizika-Kosmos'	348K [32]	5.2	0.2	20
Space Research Institute of the Russian Academy of Sciences [58]	BOKZ-M	7.5	1.4	8x8
	BOKZ-M60	7.5	0.4	8x8
	BOKZ-M60/1000	5.8	0.1	16x16
	BOKZ-MF	5.8	0.25	16x16
	BOKZ-MF01	5.8	0.15	16x16

Manufacturer	Model	Limiting Magnitude	Exposure Time (s)	FOV (deg)
	BOKZ-MF30/1002	5.8	0.04	16x16
	BOKZ-M60/2000	5.8	0.04	16x16
Sinclair Interplanetary	ST-16RT2 [36], [77]	--	--	7.5x10 half-angle
	S3S [78]	5.75	--	15x20.2
Berlin Space Technologies [79]	ST200	6	--	--
	ST400	6	--	--
Adcole Maryland Aerospace	MAI-SS Space Sextant [80]	6	--	--
KU Leuven	KU Leuven Star Tracker [81]	6	--	--
TY-Space	PST-3 [82]	5.5	--	15x12
	NST-4 [83]	5.8	--	15x12
Sodern	AURIGA [39]	--	--	--
	HYDRA [37], [84]	--	--	--
	HYDRA M [85]	--	--	--
	HYDRA TC [38]	--	--	--
	SED26 [86]	--	--	--
	SED20 [86]	--	--	--